



Multi-field modelling of hydride forming metals. Part I: Model formulation and validation



L.O. Jernkvist*, A.R. Massih

Quantum Technologies AB, Uppsala Science Park, SE-75183 Uppsala, Sweden
Malmö University, SE-20506 Malmö, Sweden

ARTICLE INFO

Article history:

Received 31 May 2013

Received in revised form 4 November 2013

Accepted 8 November 2013

Available online 24 January 2014

Keywords:

Hydrogen

Hydride

Diffusion

Embrittlement

Fracture

Phase transformation

Zirconium

Titanium

ABSTRACT

A computational model for hydrogen transport, hydrogen induced deformation and fracture in metals that form binary hydrides, such as Zr and Ti alloys, is presented. The model uses a continuum description of the two-phase (metal + hydride) material, and solves the multi-field partial differential equations for temperature and stress-directed hydrogen diffusion together with mechanical equilibrium in a three-dimensional finite element setting. Point-kinetics models are used for metal-hydride phase transformation and stress-directed orientation of hydride precipitates, while a cohesive zone fracture model caters for initiation and propagation of cracks. The local fracture properties of the hydrided material are correlated to the calculated local concentration and orientation of the hydride precipitates, which have a strong embrittling effect on the material.

In Part I of this two-part paper, we present sub-models applied for the aforementioned phenomena together with a detailed description of their numerical implementation. The applicability of the model is then demonstrated by simulating five independent experiments on hydrogen transport, metal-hydride phase transformation and stress-directed hydride orientation in zirconium alloys. Based on the results, we conclude that the model captures these phenomena over a wide range of thermo-mechanical loading conditions, including thermal cycling. Part II of the paper is focussed on fracture, and includes details on the fracture model and its validation against tests and experiments on initiation and propagation of hydride induced cracks.

© 2013 Elsevier B.V. All rights reserved.

1. Introduction

Hydrogen absorption by some transition metals may lead to precipitation of a binary metal hydride phase, MH_x , wherein x ranges from about 1.5 to 2.0 [1]. Since the metal-to-hydride phase transformation is associated with a volumetric expansion of 15–20%, the hydride formation may cause problems by swelling and geometrical distortion of structural components. However, the far most important effect of hydride precipitates is that they embrittle the material. Since the hydride phase is much more brittle than the metal, hydride precipitation may significantly degrade the material's tensile strength and ductility [2]. The metals of primary practical importance for hydride induced embrittlement and fracture are zirconium and titanium alloys, which are in widespread use in the nuclear energy industry [3] and the aerospace and marine [4] industries, respectively. Zirconium and titanium are group 4 metals, and have similar metal-hydrogen phase

systems [5]. This is illustrated by the binary phase diagrams shown in Fig. 1. In both Zr and Ti, there are two metal phases; a hexagonal closed-packed (hcp) α -phase and a body-centered cubic (bcc) β -phase. Metal hydrides exist in two stable phases: face-centered cubic (fcc) δ -hydride with $x \approx 1.6$ and face-centered tetragonal (fct) ϵ -hydride at higher hydrogen concentrations. There is also a metastable hydride phase, γ -hydride with $x \approx 1.0$ and fct-structure, which can exist at lower temperatures. For both Zr and Ti, there is a low-temperature two-phase region, in which precipitates of δ -hydride exist in a matrix of α -metal over a wide range of hydrogen concentrations. This two-phase region is crucial for hydride induced embrittlement and fracture, and it will therefore be our main focus in this paper.

A comprehensive review of the effects of hydrogen and hydrides on the mechanical properties and fracture behaviour of zirconium and titanium can be found elsewhere [2], and details on the subject will be given in Part II of our work [6]. Here, we will just summarize some characteristics of hydride embrittlement and fracture in the mixed α -metal + δ -hydride region. It is well known that the degree of embrittlement in this region depends on both the volume fraction and the orientation of the platelet-shaped precipitates of δ -hydride. At high volume fractions of hydrides, the

* Corresponding author at: Quantum Technologies AB, Uppsala Science Park, SE-75183 Uppsala, Sweden. Tel.: +46 18 509690.

E-mail addresses: loje@quantumtech.se (L.O. Jernkvist), alma@quantumtech.se (A.R. Massih).

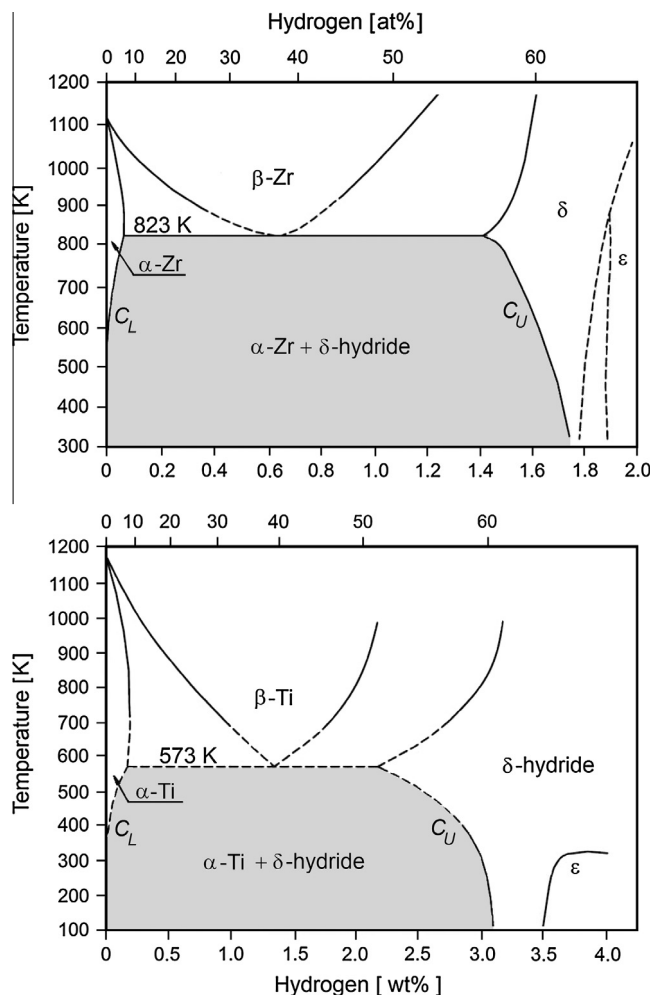


Fig. 1. Phase diagrams showing stable phases of the Zr–H and Ti–H binary systems [5]. The α -metal + δ -hydride region (shaded) is considered in the present work.

embrittlement may become severe, since crack growth is possible through a network of interconnected hydrides that provide a brittle crack path through the material. This mode of fracture is very sensitive to the hydride orientation with respect to the direction of tensile stress [7]. At low hydride concentration, a continuous crack path through the brittle hydride phase cannot be formed. Still, the material may lose much of its macroscopic ductility, since the hydrides hinder plastic deformation (dislocation movements) and/or promote initiation and link-up of voids in the material [8].

In addition to these embrittling effects, hydride formation may also challenge the structural integrity through slow, sub-critical fracture processes. This is because hydrogen atoms in solid solution diffuse towards regions with high hydrostatic stress, which over time may lead to excessive local hydride formation ahead of stress-concentrators, such as notches and cracks. Ultimately, the locally embrittled and stressed region may fail, leading to a short (10–20 μm) increment of crack growth. The process then repeats itself, thus giving rise to stable crack growth, the rate of which is basically controlled by the rate of hydrogen diffusion to the peak stress region.

Hydride formation may thus jeopardize the structural integrity of the material in many ways. Accurate computational models are therefore needed, by which hydride induced failures can be predicted, given the loading and environment conditions of a specific component over time. As of today, such models are usually restricted to a specific failure mechanism in a specific material.

Moreover, current models are restricted to simple loading and environment conditions, such as constant and uniaxial loading of a material with constant and uniform temperature. To our knowledge, models for hydride induced embrittlement and fracture under general conditions are as yet unavailable. The reason is that, in a general case, several phenomena have to be considered and modelled simultaneously: (i) Hydrogen diffusion, driven by gradients in stress, temperature and hydrogen concentration. (ii) Metal-hydride phase transformation, i.e. precipitation and dissolution of hydrides. (iii) Stress-directed orientation of hydride precipitates, which induces a very strong directional dependence (anisotropy) for the expansion and strength of hydrided material. (iv) Expansion of the material, caused by hydrogen in solid solution within the metal as well as hydride precipitates, and resulting in internal (misfit) stresses. (v) Cracking and fracture of hydrided material.

Although sub-models exist in the literature for the aforementioned phenomena, there are very few reported attempts to combine these sub-models into comprehensive computational models for hydride induced fracture. This work is an attempt in that direction. Here, we integrate phenomenological sub-models for hydrogen diffusion, metal-hydride phase transformation, stress-directed hydride orientation, hydrogen induced expansion, and fracture of hydride-embrittled materials by coupling the governing equations for the involved phenomena. The resulting system of multi-field partial differential equations (PDEs) is then solved numerically by use of the finite element method. The outcome is a flexible numerical model, which can be used to study a wide range of problems involving temperature- and/or stress-directed transport of hydrogen in combination with hydride precipitation and fracture. The model, which uses a continuum mechanics approach with relevant length scales from microns to centimetres, may also help to bridge the gap between mesoscale models and engineering approaches to fracture in hydride forming metals.

Part I of this two-part paper deals mainly with the formulation and numerical implementation of the model. In addition, results of model validation against experiments on hydrogen transport, metal-hydride phase transformation and stress-directed hydride orientation are presented. Part II of the work [6] is focussed on fracture, and includes details on the fracture model and its validation against tests and experiments on initiation and propagation of hydride induced cracks. Part I of the paper is organized as follows: Section 2 presents a set of sub-models, applied for modelling the fundamental phenomena discussed in the introduction. Section 3 deals with the numerical implementation and integration of the sub-models. The end result is a three-dimensional finite-element based solution to the space-time variations of hydrogen and hydride concentration, hydride orientation, stress and strain. In Section 4, key elements of the model are validated against well-defined separate effect tests and experiments on the behaviour of hydrogen and hydrides in zirconium alloys. Discussions of the model, including comparisons with other modelling approaches, are given in Section 5, and the conclusions are finally summarized in Section 6.

2. Model description

2.1. Representation of hydrided material

In optical microscopy, precipitates of δ -hydride in α -phase Ti and Zr alloys usually appear as thin discs or platelets, and in polycrystalline materials, they exist both within the grains and on grain boundaries [1]. These macroscopic hydrides (2–10 μm wide and 0.1–0.2 μm thick) are reported to consist of smaller precipitates (0.1–0.2 μm wide and 30–50 nm thick), which are closely stacked

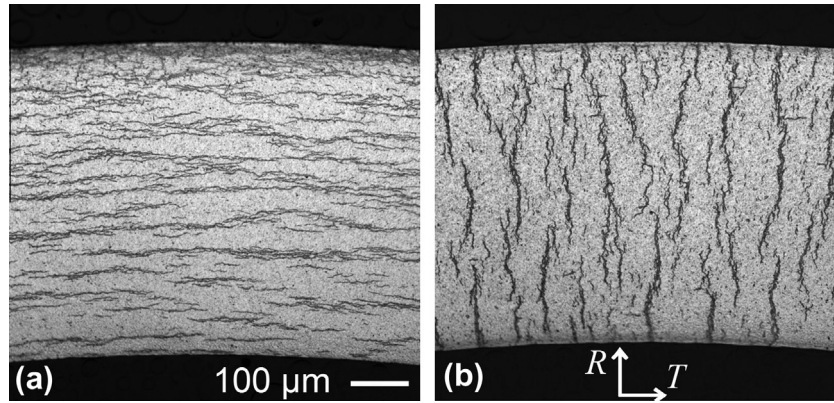


Fig. 2. Illustration of (a) circumferential and (b) radial δ -hydrides in a zirconium alloy tube. Cross-sectional micrograph of the tube wall with the radial (R) and tangential (T) directions of the tube indicated. Circumferential hydrides precipitate under stress-free conditions, whereas radial hydrides form under tangential tensile stress. Micrographs reprinted from [10], with permission from Elsevier.

and aligned with the overall orientation of the macroscopic hydride [9]. In stress-free conditions, most materials show a clear preferential hydride orientation, which depends primarily on the material's grain structure and texture, which, in turn, depend on the manufacturing route. For instance, plates, sheets and tubes are usually manufactured by hot working, employing rolling or extrusion, followed by cold working through rolling or pilgering. This produces a material where, in absence of externally applied stress, the preferential planes for hydride precipitation tend to coincide with the principal directions of cold work. Under applied stress, the preferred hydride orientation will change [10]. Hydrides in tubes are therefore often characterized simply as “circumferential” or “radial”, as illustrated in Fig. 2. Detailed studies of the hydride morphology can be found in [11–13] for zirconium alloys and in [14,15] for α -titanium.

In our model, we use a continuum description for the hydrided material, whereby the platelet-shaped δ -hydride precipitates are represented by two internal variables for the local state of the material: the hydride volume fraction, κ , and the hydride mean orientation, θ_i , where $i = 1, 2, 3$. The latter variables define the fractions of hydride platelets having their normals aligned with the coordinate directions, as illustrated in Fig. 3. The coordinate directions (x_1, x_2, x_3) are assumed to be aligned with the principal directions of cold work.

The internal state variables κ and θ_i are local properties. They are treated as key parameters in calculations of the local strength, toughness and expansion of the two-phase (α -metal + δ -hydride) material, and they also have an impact on the hydrogen transport within the material. The space–time variations of κ and θ_i are in the model calculated from the space–time variations of temperature and stress through sub-models described in Sections 2.2–2.4.

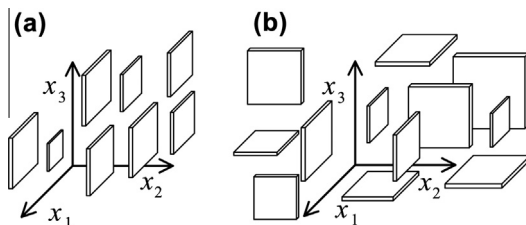


Fig. 3. Illustration of the variables θ_i , which define the mean orientation of δ -hydride precipitates. (a) Material with $\theta_2 = 1$, meaning that all hydrides are oriented with their normals aligned with x_2 . (b) Material with random hydride orientation, i.e. $\theta_1 = \theta_2 = \theta_3 = 1/3$.

2.2. Hydrogen transport

Assuming that there is no hydrogen production within the material, the balance of hydrogen in a certain point of the material is given by the continuity equation

$$\frac{dC}{dt} + \text{div} \vec{J} = 0, \quad (1)$$

where C is the total hydrogen concentration, t is the time, and \vec{J} is the hydrogen flux vector. The total hydrogen concentration includes free hydrogen, i.e. interstitial hydrogen atoms in solid solution, as well as hydrogen that is chemically bound in δ -hydride precipitates. Hence, we write

$$C = (1 - \kappa)C_s^m + \kappa(C_s^h + C_b) = C_s + \kappa C_b, \quad (2)$$

where C_s^m and C_s^h are the concentrations of hydrogen in solid solution within the metal and hydride phases, respectively¹, and C_b is the concentration of chemically bound hydrogen within the hydride phase. $C_s = (1 - \kappa)C_s^m + \kappa C_s^h$ is the average concentration of free hydrogen in the two-phase material. Hence, unlike most other models of this kind in the literature, it is here assumed that free hydrogen exists not only in the metal but also in the hydride phase and that $\vec{J} \neq 0$ in the hydride precipitates. Consequently, the total hydrogen flux in Eq. (1) comprises contributions from both phases. It should be remarked that the division of hydrogen in the hydride phase into either free (C_s^h) or chemically bound (C_b) hydrogen is artificial, but it is necessary for making the model applicable to materials consisting of pure hydride phase ($\kappa = 1$). For reasons of local equilibrium at the metal-to-hydride interface, it is assumed that the concentrations of free hydrogen in the hydride and metal phases are comparable. More precisely, it is assumed that $C_s^h = c C_s^m$, where $c \in [0, 1]$ is a dimensionless model parameter that defines the jump of free hydrogen concentration at the metal-to-hydride interface. This model parameter is further discussed in Section 5.1.2.

Making use of Einstein's summation convention (repeated subscripts implies summation over spatial coordinates), we calculate the components of the total flux vector from

$$J_k = (\delta_{kl} - A_{kl})J_l^m + A_{kl}J_l^h, \quad (3)$$

where J_l^m and J_l^h are the molar fluxes of hydrogen in metal and hydride, respectively, δ_{kl} is the Kronecker delta, and A_{kl} is a diagonal, dimensionless tensor, whose components generally depend on both

¹ Henceforth, superscripts m and h will be used for properties of the metal and hydride phase, respectively.

κ and θ_i ; see Fig. 3. More exactly, the diagonal component $A_{kk} \in [0, 1]$ is the fraction of hydrides on the projected area perpendicular to the k :th direction. Since $J_i^h \ll J_i^m$, the flow of hydrogen through the two-phase material is hindered by hydride precipitates. The strongest reduction of the hydrogen flux is obtained when the flux vector is normal to the hydride platelets. For example, hydrogen flowing in the x_2 -direction in Fig. 3 will experience the strongest resistance from the hydride morphology shown in Fig. 3a. In case $\theta_1 = \theta_2 = \theta_3 = 1/3$, or if the dependency of hydride orientation is neglected, $A_{kl} = \kappa \delta_{kl}$.

For each of the partial molar fluxes in Eq. (3), we apply a widely used constitutive relation for temperature- and stress-directed diffusion [16]

$$J_l^\omega = -D^\omega \left(\frac{\partial C_s^\omega}{\partial x_l} + \frac{C_s^\omega Q^{*\omega}}{RT^2} \frac{\partial T}{\partial x_l} + \frac{C_s^\omega V^{*\omega}}{RT} \frac{\partial p}{\partial x_l} \right), \quad (4)$$

where R is the universal gas constant, T is the absolute temperature and p is the hydrostatic pressure. The latter is defined by $p = -\text{tr}(\sigma_{kl})/3$, where σ_{kl} is the Cauchy stress tensor. Superscript ω in Eq. (4) denotes either the metal (m) or hydride (h) phase, see Eq. (3), and D^ω , $Q^{*\omega}$ and $V^{*\omega}$ are the hydrogen diffusivity, heat of transport and volume of transport for each phase. Eq. (4) is an expanded form of the general diffusion equation $\vec{J} = -DC_s \nabla \mu / RT$, where $\nabla \mu$ is the gradient of the chemical potential of hydrogen in the material [17,18].

Combining Eqs. (1)–(4), we find a time-dependent, partial differential equation, which contains the free hydrogen concentration and the hydride volume fraction as primary unknowns. To solve this equation with respect to time and space, we need a model for the metal-hydride phase transformation kinetics, by which the hydride volume fraction can be calculated.

2.3. Metal-hydride phase transformation

Under moderate rates of cooling or heating, precipitation and dissolution of δ -hydride in Ti and Zr and their alloys are diffusion-controlled processes, for which temperature has a strong effect on the kinetics [19]. For example, precipitation proceeds by diffusion of interstitial hydrogen atoms to dislocations and/or grain boundaries, where hydrides nucleate and grow. Here, we use a point-kinetics phase transformation model, which is analogous to that derived by Ham [20] for precipitation on a periodic array of dislocations. Hence, we write the local rate of change for the δ -hydride volume fraction as

$$\frac{d\kappa}{dt} + \frac{1}{\tau}(\kappa - \kappa_e) = 0, \quad (5)$$

where τ is a characteristic time and κ_e is the hydride volume fraction under equilibrium conditions, i.e. the hydride volume fraction that would be reached after infinite time, if the current conditions were held constant. The latter property can be calculated from the phase diagram for the metal-hydrogen system by use of the lever rule

$$\kappa_e = \frac{C - C_L}{C_U - C_L}, \quad \text{if } C_L \leq C \leq C_U. \quad (6)$$

Here, C is the total hydrogen concentration in the material and C_L and C_U denote the lower and upper boundary, respectively, to the mixed α -metal + δ -hydride region of the phase diagram; see Fig. 1. Hence, C_L is the terminal solid solubility of hydrogen in the α -phase metal, and C_U is the lower limit concentration of hydrogen in pure δ -hydride phase. C_L and C_U are material properties that depend strongly on temperature. C_L also depends on the direction of phase transformation, as will be further discussed below.

The characteristic time τ in Eq. (5) is strongly temperature dependent and follows the relation $\tau \propto l_s^2/D^m$, where l_s is a

microstructural length, reflecting the typical length for hydrogen diffusion in the phase transformation process [20]. For hydride precipitation, l_s can be viewed as the typical spacing of preferred nucleation sites for hydrides in the material, such as dislocations and grain boundaries. In case of dissolution, l_s is a measure of the precipitate size [21]. In our model, we calculate τ from

$$\tau = l_s^2/D^m, \quad (7)$$

where l_s is treated as a material-dependent constant, and the hydrogen diffusivity in the metal phase, D^m , is correlated to local temperature. The validity of Eq. (7) has been verified experimentally for both dissolution [21] and precipitation [22–25] of hydrides in zirconium alloys.

We note that Eq. (5) is a first order approximation, the limitations of which will be discussed in Section 5.1.3. Most importantly, Eq. (5) is applicable only to materials for which the phase equilibrium given by κ_e in Eq. (6) is unambiguously defined by the current state, i.e. to materials in which the boundaries to the mixed metal + hydride phase region are path-independent. Such materials hardly exist: The hydrogen solubility limit C_L under hydride dissolution (heating) is known to be different from that under precipitation (cooling) for most hydride forming metals, including Ti and Zr alloys [26]. It is generally believed that this hysteresis in hydrogen solubility is caused by elasto-plastic accommodation of the material's volume change during hydride dissolution or precipitation [27]. Hence, for a more realistic description of the phase transformation kinetics, we replace Eq. (5) with

$$\frac{d\kappa}{dt} + \frac{1}{\tau_d}(\kappa - \kappa_d) = 0 \quad \text{if } \kappa > \kappa_d, \quad (8a)$$

$$\frac{d\kappa}{dt} + \frac{1}{\tau_p}(\kappa - \kappa_p) = 0 \quad \text{if } \kappa < \kappa_p, \quad (8b)$$

$$\frac{d\kappa}{dt} = 0 \quad \text{if } \kappa_p \leq \kappa \leq \kappa_d. \quad (8c)$$

Here, κ_d and κ_p are the phase equilibria for hydride dissolution and precipitation. They are calculated from Eq. (6) by setting C_L equal to the hydrogen terminal solid solubility limit under hydride dissolution (C_L^{TSSD}) and precipitation (C_L^{TSSP}), respectively. It is clear from Eq. (8) that the unique phase equilibrium defined by κ_e in Eq. (5) is here replaced by a region of equilibrium, defined by $\kappa_p \leq \kappa \leq \kappa_d$. This region corresponds to the hysteresis in hydrogen solubility between hydride dissolution and precipitation. We also note from Eq. (8) that the characteristic time for hydride precipitation, τ_p , may be different from that for dissolution, τ_d . This will be further discussed in Section 5.1.3.

2.4. Stress-directed orientation of hydride precipitates

Theoretical as well as experimental studies on hydride precipitation in Ti and Zr alloys suggest that the stress-directed orientation of δ -hydride platelets occurs through orientation of nuclei rather than through selective growth of stable nuclei [19,28]. This is consistent with the observation that the hydride platelets are composed of submicron size precipitates that are closely stacked and aligned; see Section 2.1. Consequently, we calculate the rate of change for the hydride mean orientation from a nucleation-based model, which means that the mean orientation of hydride platelets is assumed to change only when new δ -hydrides nucleate with an orientation that differs from that of the existing population.

Following the material description in Section 2.1, the volume fraction of δ -hydride platelets aligned with the i :th coordinate axis, κ_i , is simply $\kappa_i = \kappa \theta_i$. Here, we make the fundamental ansatz

$$\frac{d\kappa_i}{dt} = [\theta_i \Omega(\kappa) + \eta_i (1 - \Omega(\kappa))] \frac{d\kappa}{dt}, \quad \text{if } \frac{d\kappa}{dt} > 0, \quad (9)$$

where η_i is the fraction of hydrides nucleated in the i :th direction at a given instant, and $\Omega(\kappa)$ is a dimensionless empirical function. It is continuously increasing in the interval $0 \leq \kappa \leq 1$, and satisfies $\Omega(0) = 0$ and $\Omega(1) = 1$. As will be shown below, η_i is a function of the current temperature and stress state, and it also depends on the density of precipitate habit planes aligned in the i :th direction. The latter quantity is linked to microstructural properties of the material, e.g. the texture and grain shape.

The ansatz in Eq. (9) implies that the hydride mean orientation will change by nucleation of new hydrides with an orientation given by the current temperature and stress when there are very few existing hydrides in the material. In that case, both κ and $\Omega(\kappa)$ are close to zero. However, in a material with a more significant amount of hydrides, the hydride volume fraction increases by growth of already existing hydrides, rather than by nucleation of new precipitates. In this case, $\Omega(\kappa) \approx 1$, and the change in hydride mean orientation is negligible.

Since $\kappa_i = \kappa \theta_i$, its time derivative is

$$\frac{d\kappa_i}{dt} = \kappa \frac{d\theta_i}{dt} + \theta_i \frac{d\kappa}{dt}. \quad (10)$$

By combining Eqs. (9) and (10), we get the rate of change for the hydride mean orientation

$$\frac{d\theta_i}{dt} = (1 - \Omega(\kappa)) \frac{(\eta_i - \theta_i)}{\kappa} \frac{d\kappa}{dt} \quad \text{if } \frac{d\kappa}{dt} > 0. \quad (11)$$

We note that $d\theta_i/dt \neq 0$ only when $d\kappa/dt > 0$ in our model, i.e. the hydride mean orientation changes as a result of hydride nucleation only. If hydrides dissolve, $d\kappa/dt < 0$, and θ_i are unchanged. This means that the rate of dissolution is supposed to be the same for all hydrides, irrespective of their orientation. The hydride orientation model given by Eq. (11) is validated against experimental data in Section 4.5, and discussed in Section 5.3.

The fraction of δ -hydrides nucleated in the i :th direction depends on the current stress state and temperature. It is calculated through an expression derived from classical theory of homogeneous nucleation

$$\eta_i(T, \sigma_{kl}) = \frac{n_{oi} \exp(\mathcal{V}_c^h \varepsilon_{kl}^{Tj} \sigma_{kl} / k_B T)}{\sum_{j=1}^3 n_{oj} \exp(\mathcal{V}_c^h \varepsilon_{kl}^{Tj} \sigma_{kl} / k_B T)}. \quad (12)$$

Here, n_{oi} is the fraction of hydrides nucleated in the i :th direction under stress-free conditions, σ_{kl} is the Cauchy stress tensor, \mathcal{V}_c^h is the volume of a critical size hydride nucleus, k_B is the Boltzmann constant, and ε_{kl}^{Tj} is the transformation (misfit) strain tensor for a δ -hydride platelet oriented with its normal in the i :th direction. Eq. (12) is derived in Appendix A.

2.5. Material deformation

The material is in our model assumed to deform by elasticity, viscoplasticity and creep, and to expand by thermal dilatation, interstitial hydrogen and hydride precipitates. The constitutive relation for the material is

$$\dot{\sigma}_{ij} = C_{ijkl} (\dot{\varepsilon}_{kl} - \dot{\varepsilon}_{kl}^{th} - \dot{\varepsilon}_{kl}^{hy} - \dot{\varepsilon}_{kl}^{pl} - \dot{\varepsilon}_{kl}^{cr}), \quad (13)$$

where (\cdot) denotes time derivative, ε_{kl} is the total strain tensor, and superscripts th, hy, pl and cr refer to strains arising from thermal expansion, hydrogen induced expansion, plasticity and creep. The stiffness tensor C_{ijkl} is that for an elastically isotropic material, i.e. $C_{ijkl} = \lambda \delta_{ij} \delta_{kl} + G(\delta_{ik} \delta_{jl} + \delta_{il} \delta_{jk})$, where λ and G are the Lamé coefficients [29]. These coefficients will in a general case depend on

hydride content. However, δ -hydrides in group 4 metals have about the same elastic properties as the α -phase base metal [30,31], which means that the compositional dependence of λ and G can be neglected for this hydride phase.

Also the thermal expansion is assumed to be isotropic, and calculated through $\dot{\varepsilon}_{kl}^{th} = \alpha(\kappa) \dot{T} \delta_{kl}$, where \dot{T} is the temperature rate of change and $\alpha(\kappa)$ is the coefficient of thermal expansion for the two-phase material. It is calculated from a rule of mixture, $\alpha(\kappa) = (1 - \kappa) \alpha^m + \kappa \alpha^h$, where α^m and α^h are the coefficients for pure metal and hydride phase, respectively.

The material is assumed to expand isotropically by hydrogen in solid solution and anisotropically by precipitation of δ -hydrides. More precisely, the rate of change for the hydrogen induced strain is calculated through

$$\dot{\varepsilon}_{kl}^{hy} = \frac{d}{dt} \left(\frac{(1 - \kappa) C_s^m \bar{V}^{Hm}}{3} \delta_{kl} + \kappa \sum_{j=1}^3 \theta_j \varepsilon_{kl}^{Tj} \right), \quad (14)$$

where \bar{V}^{Hm} is the partial molar volume of hydrogen in the metal. It should be remarked that the expansion caused by hydrogen in solid solution is actually anisotropic for metals with hcp structure [32]. However, at the temperatures considered here ($T < 650$ K), the expansion caused by hydrogen in solid solution is small, and we therefore neglect this anisotropy.

Non-elastic deformation by both viscoplasticity and creep is considered in the model. By definition, viscoplasticity occurs only when the yield strength of the material is transgressed, whereas creep takes place also at low stress. Since both modes of deformation are considered, the model is applicable to a wide range of thermo-mechanical loading conditions and time scales.

2.6. Fracture

Fracture, i.e. initiation and propagation of cracks, is modelled by allowing separation of the material along pre-defined crack planes. Fracture is thus treated by use of a cohesive zone model, which is implemented in the finite element computational framework. As illustrated in Fig. 4, fracture processes, leading to decohesion of the material, are assumed to take place in a finite-size fracture

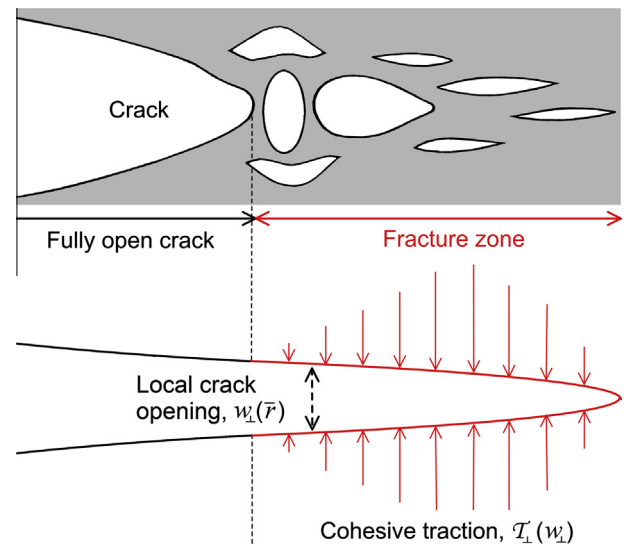


Fig. 4. Illustration of the cohesive zone fracture model. Separation of the material at the crack front is resisted by cohesive tractions, T_i , which depend on the local crack opening (displacement jumps across the crack plane), w_j . For simplicity, the figure is drawn for mode I loading (symmetric opening load). In this case, all components of T_i and w_j are zero, except for the components perpendicular to the crack plane (T_\perp and w_\perp).

zone rather than at a distinct crack front. The decohesion is restricted by cohesive tractions, T_i . These tractions, which act as cohesive forces at the crack front, depend on the local separation of the crack faces, w_j , and on the local state of the material, i.e. on temperature, hydride concentration, hydride orientation, etc. The fracture process is thus described mathematically by a decohesion law, $T_i(w_j)$, which depends on κ , θ_i and other local state variables for the material at the crack front. The decohesion law $T_i(w_j)$ is further described in [Appendix B](#), and in Part II [\[6\]](#).

3. Numerical implementation

The governing equations to be solved are the hydrogen transport equation, including metal-hydride phase transformation, and the equations for mechanical equilibrium, including hydrogen induced deformation and fracture of hydride-rich material. These time-dependent PDEs are discretized in space by use of the finite element method, and implicit time stepping (backward Euler method) is used for the discretization with respect to time. We have chosen to solve the discretized equations for hydrogen transport and mechanical equilibrium separately and incrementally, as shown in [Fig. 5](#). Iterations are usually required in each time step to cater for the interconnection between the hydrogen transport problem and the mechanical behaviour of the structure: The solution to the hydrogen transport problem relies on stresses and stress gradients calculated in the mechanical analyses, and conversely, the calculated distributions of free hydrogen, hydride volume fraction and hydride mean orientation are needed in mechanical analyses to define hydrogen induced strains and material strength. In fact, iterations are usually needed also when this interconnection is disregarded, since the governing equations for hydrogen transport and mechanical equilibrium are, as such, nonlinear.

The iterations are terminated when both solutions have converged, and the differences in calculated results from two successive iterations become less than user-defined tolerances. The latter condition is important, since it ensures consistency between the converged solutions reached separately in the hydrogen transport and mechanical analyses. Once a globally converged solution is reached, the solution is advanced to a new time step. The time step length is set adaptively, so that the change of certain key variables from one time step to another should nowhere exceed pre-defined limits. Among these variables are temperature,

effective strains from viscoplasticity and creep, free hydrogen concentration and hydride volume fraction.

The reasons for solving the PDEs for hydrogen transport and mechanical equilibrium separately, rather than solving them simultaneously, are discussed in [Section 5.2](#). Here, we note that the same finite element mesh is used for the hydrogen transport and mechanical problem, and that the same low-level finite element procedures are used in both solutions. We also note that the space–time variation of temperature is supplied as input, and not calculated within the model. Thermal feedback effects from material deformation and metal-hydride phase transformation are thus assumed to be negligible. The following subsections present the solution procedures for the PDEs for hydrogen transport and mechanical equilibrium, respectively.

3.1. Hydrogen transport equations

Let us start by re-writing [Eq. \(1\)](#) in the form

$$\frac{d}{dt}(C_s + \kappa C_b) + J_{k,k} = 0, \quad (15)$$

where $C_s = (1 - \kappa)C_s^m + \kappa C_s^h$ is the average concentration of hydrogen in solid solution within the hydridized material, and the shorthand notation y_k means $\partial y / \partial x_k$. As before, repeated subscripts imply summation over spatial coordinates.

The solution strategy for [Eq. \(15\)](#) is to treat C_s as the primary unknown, and to apply the finite element method to obtain a system of linear equations for the time increments of C_s in element nodes. It should be remarked that the solution is derived specifically for the constitutive relation in [Eq. \(4\)](#) and the phase transformation model described by [Eq. \(8\)](#). However, with some modification, the solution strategy can be adapted to other models for hydrogen diffusion and metal-hydride phase transformation.

3.1.1. Discretization with respect to time

Consider a time step of length Δt , beginning at time t and ending at $t + \Delta t$. Then, the time discretized form of [Eq. \(15\)](#) may be written as

$$\frac{\Delta C_s}{\Delta t} + \frac{(\kappa C_b)^{t+\Delta t} - (\kappa C_b)^t}{\Delta t} + J_{k,k} = 0, \quad (16)$$

where superscripts t and $t + \Delta t$ refer to the points in time for which the product κC_b is evaluated. Next, we decompose the variables at the advanced time $t + \Delta t$ into already known quantities at time t and unknown increments $\Delta \kappa$, ΔC_b :

$$\kappa^{t+\Delta t} = \kappa^t + \Delta \kappa, \quad C_b^{t+\Delta t} = C_b^t + \Delta C_b. \quad (17)$$

Moreover, we will apply an implicit (backward Euler) time stepping scheme, meaning that the hydrogen flux in [Eq. \(16\)](#) is evaluated at the advanced time $t + \Delta t$. Accordingly, by substituting [Eq. \(17\)](#) into [Eq. \(16\)](#), we get

$$\frac{\Delta C_s}{\Delta t} + \frac{C_b^t \Delta \kappa + \Delta C_b \kappa^{t+\Delta t}}{\Delta t} + J_{k,k}^{t+\Delta t} = 0. \quad (18)$$

For the sake of generality, we assume that the concentration of hydrogen that is chemically bound in the hydride phase, C_b , depends on temperature. For a material that consists of pure δ -hydride, $\kappa = 1$, $C_s = C_s^h$, and $C = C_U$, which inserted into [Eq. \(2\)](#) yields $C_b = C_U - C_s$. Hence, C_b is related to the upper boundary of the mixed α -metal + δ -hydride region of the phase diagram, C_U , which is here supposed to be a known function of temperature; see [Fig. 1](#) and [Section 2.3](#).

Substituting $\Delta C_b = \Delta C_U - \Delta C_s$ into [Eq. \(18\)](#), we get

$$\frac{\Delta C_s(1 - \kappa^{t+\Delta t})}{\Delta t} + \frac{C_b^t \Delta \kappa + \Delta C_U \kappa^{t+\Delta t}}{\Delta t} + J_{k,k}^{t+\Delta t} = 0. \quad (19)$$

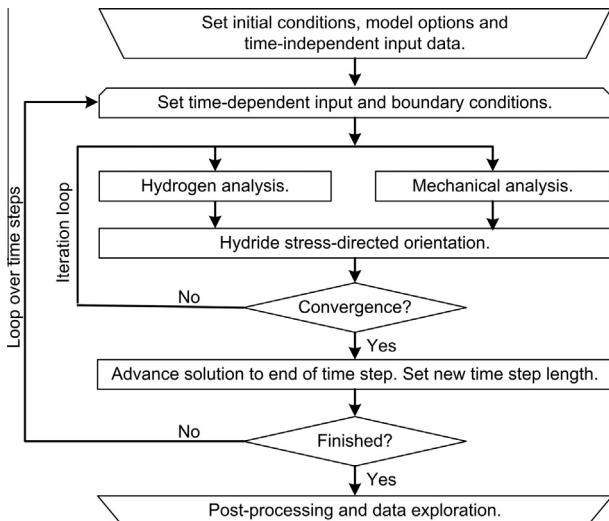


Fig. 5. Flowchart illustrating the numerical solution strategy.

Since ΔC_U can be calculated directly from the known change in temperature during the time step, the unknown quantities in Eq. (19) are the increments ΔC_s and $\Delta \kappa$, and also the hydrogen flux at the advanced time, $J_k^{t+\Delta t}$. We note that $\Delta \kappa$ and $J_k^{t+\Delta t}$ may depend strongly on the primary unknown ΔC_s , and efficient numerical solution of Eq. (19) therefore requires that $\Delta \kappa$ and $J_k^{t+\Delta t}$ can be expressed in terms of ΔC_s . With the phase transformation models in Section 2.3, $\Delta \kappa$ can be written as

$$\Delta \kappa = Y^I \Delta C_s - Y^{II}, \quad (20)$$

where the functions Y^I and Y^{II} are defined in Appendix C. Likewise, with the hydrogen diffusion model in Section 2.2, we may write $J_k^{t+\Delta t}$ as a linear combination of ΔC_s and $\Delta C_{s,k}$

$$J_k^{t+\Delta t} = -X^I \Delta C_{s,k} - X_k^{II} \Delta C_s - X_k^{III}, \quad (21)$$

where X^I , X_k^{II} and X_k^{III} are functions that involve fundamental material properties for hydrogen diffusion; see Appendix D.

3.1.2. Discretization with respect to space

An approximate solution to Eq. (1) can be found by requiring that

$$\int_V \psi \left[\frac{dC}{dt} + \text{div} \vec{J} \right] dV = 0, \quad (22)$$

where ψ is a finite set of trial functions, which are linearly independent over the integration volume V . Here, we will apply the finite element method, in which the trial functions are identical to the element shape functions, i.e. the low-order polynomials (interpolants) used for representation of field variables within each finite element [33].

Hence, we consider a finite element with volume V_e and boundary surface S_e . By replacing the hydrogen balance equation within brackets in Eq. (22) with its time-discretized counterpart from Eq. (19) and performing the integration over the considered element, we get

$$\begin{aligned} \int_{V_e} \psi \left[\frac{\Delta C_s (1 - \kappa^{t+\Delta t})}{\Delta t} + \frac{C_b^t \Delta \kappa + \Delta C_U \kappa^{t+\Delta t}}{\Delta t} \right] dV \\ = - \int_{S_e} \psi J_k^{t+\Delta t} n_k dS + \int_{V_e} \psi_{,k} J_k^{t+\Delta t} dV, \end{aligned} \quad (23)$$

where n_k is the outward surface normal to the element boundary surface S_e . The right-hand side terms in Eq. (23) were obtained by integrating the hydrogen flux by parts and applying the divergence theorem. The first term on the right-hand side involves integration of the outward hydrogen flux over S_e . This flux can be assumed to be known from given boundary conditions.

Next, we combine Eqs. (20) and (21) with Eq. (23). The result is

$$\begin{aligned} \int_{V_e} \psi \left[\frac{\Delta C_s \left[1 - \kappa^t + Y^I (C_b^t + \Delta C_U - \Delta C_s) + Y^{II} \right]}{\Delta t} \right] dV \\ + \int_{V_e} \psi_{,k} X^I \Delta C_{s,k} dV + \int_{V_e} \psi_{,k} X_k^{II} \Delta C_s dV \\ = - \int_{S_e} \psi J_k^{t+\Delta t} n_k dS - \int_{V_e} \psi \left[\frac{\Delta C_U \kappa^t - Y^{II} (C_b^t + \Delta C_U)}{\Delta t} \right] dV \\ - \int_{V_e} \psi_{,k} X_k^{III} dV. \end{aligned} \quad (24)$$

Here, the three terms on the left-hand side contain the primary unknown ΔC_s or its gradient. The first term is nonlinear in ΔC_s , but the nonlinearity is weak, since $|C_b^t + \Delta C_U| \gg |\Delta C_s|$. However, the nonlinearity requires that Eq. (24) is solved iteratively. Thus, we replace ΔC_s within parentheses in the first term of Eq. (24) with ΔC_s^0 , which

denotes the increment of C_s calculated in the previous iteration cycle.

Following the common procedure in finite element methods, the spatial variation of the unknown ΔC_s and the trial function ψ within an element is approximated by interpolation in the element nodal values with the help of element shape functions, $H_q(\vec{r})$, where subscript q refers to the q :th node of the element and \vec{r} is the spatial position. Hence, within the element, a field variable y and its partial derivatives are calculated from

$$y(\vec{r}, t) = \sum_{q=1}^N H_q(\vec{r}) y^q(t), \quad \text{and} \quad y_{,k}(\vec{r}, t) = \sum_{q=1}^N H_{q,k}(\vec{r}) y^q(t), \quad (25)$$

where y^q is the value of y in node q , and N is the number of nodes in the element. Using Eq. (25) for both ΔC_s and ψ in Eq. (24), we arrive at a system of linear equations for the concentration increments of hydrogen in solid solution at element nodes, ΔC_s^q :

$$\sum_{q=1}^N K^{pq} \Delta C_s^q = F^p - Q^p. \quad (26)$$

The element system matrix K^{pq} can be viewed as a sum of three parts, defined by

$$^I K^{pq} = \int_{V_e} \left[1 - \kappa^t + Y^I (C_b^t + \Delta C_U - \Delta C_s^0) + Y^{II} \right] \frac{H_p H_q}{\Delta t} dV, \quad (27a)$$

$$^{II} K^{pq} = \int_{V_e} X^I H_{p,k} H_{q,k} dV, \quad (27b)$$

$$^{III} K^{pq} = \int_{V_e} X_k^{II} H_{p,k} H_{q,k} dV. \quad (27c)$$

We note that $^I K^{pq}$ depends on ΔC_s^0 , which is the increment of C_s , calculated in a previous iteration step. Moreover, $^{III} K^{pq}$ is unsymmetric, which means that the total element system matrix K^{pq} is also unsymmetric. The two terms on the right-hand side of Eq. (26) can be interpreted as “loads” associated with the element nodes. For the p :th node, these loads are

$$F^p = - \int_{S_e} H_p J_k^{t+\Delta t} n_k dS, \quad (28a)$$

$$Q^p = \int_{V_e} \left[\left(\Delta C_U \kappa^t - Y^{II} (C_b^t + \Delta C_U) \right) \frac{H_p}{\Delta t} + X_k^{III} H_{p,k} \right] dV. \quad (28b)$$

Here, F^p represent element nodal loads that arise from a prescribed hydrogen flux across the element boundary, whereas Q^p are element equivalent nodal loads. In case there are no prescribed fluxes across the element boundary, $F^p = 0$.

The integrals in Eqs. (27) and (28) are evaluated by recourse to numerical quadrature, using standard methods for isoparametric finite elements [33]. The system matrix and load vector for each element are assembled with contributions from all other elements in the structure, resulting in a global, unsymmetric, system of linear equations for the unknown nodal increments of C_s . We solve this system by use of the HSL MA42_ELEMENT frontal solver [34]. Iterations are needed in each time step, since the system matrix as well as the nodal loads depend on the unknown end-of-time-step values for C_s and κ . Increments for κ are in each iteration calculated from Eq. (8), which is applied locally in each integration (gauss) point of each finite element.

3.2. Mechanical equilibrium equations

The governing equation for mechanical equilibrium is the principle of virtual work, which for an arbitrary body with volume V may be written

$$\int_V \sigma_{ij} \delta \varepsilon_{ij} dV - \int_{S^c} T_i \delta w_i dS = \int_V b_i \delta u_i dV + \int_{S^x} t_i \delta u_i dS, \quad (29)$$

where δu_i are virtual displacements and $\delta \varepsilon_{ij} = (\delta u_{ij} + \delta u_{ji})/2$ are virtual engineering strains, associated and compatible with δu_i . The second term on the left-hand side of Eq. (29) is the contribution from cohesive tractions, T_i , acting on the crack surface S^c ; see Section 2.6. The virtual displacement jumps across the crack, δw_i , are compatible with δu_i . The right-hand side of Eq. (29) contains applied loads in the form of body forces b_i , and tractions t_i on the external surface S^x . All integrals in Eq. (29) extend over the original volume and surface of the body, meaning that the geometry is assumed unaffected by the imposed virtual displacements.

3.2.1. Discretization with respect to time

With the aim to find an incremental solution to Eq. (29), we decompose the Cauchy stress tensor σ_{ij} and the cohesive tractions T_i at the advanced time $t + \Delta t$ into already known quantities at time t and unknown increments $\Delta \sigma_{ij}$ and ΔT_i :

$$\sigma_{ij}^{t+\Delta t} = \sigma_{ij}^t + \Delta \sigma_{ij}, \quad T_i^{t+\Delta t} = T_i^t + \Delta T_i. \quad (30)$$

The unknown increments $\Delta \sigma_{ij}$ are estimated from Eq. (13). Hence,

$$\Delta \sigma_{ij} = C_{ijkl} (\Delta \varepsilon_{kl} - \Delta \varepsilon_{kl}^{th} - \Delta \varepsilon_{kl}^{hy} - \Delta \varepsilon_{kl}^{pl} - \Delta \varepsilon_{kl}^{cr}). \quad (31)$$

Likewise, estimates for ΔT_i are given by

$$\Delta T_i = \frac{\partial T_i}{\partial w_j} \Delta w_j. \quad (32)$$

By combining Eqs. (29)–(32), we get the equilibrium equations at the advanced time $t + \Delta t$

$$\begin{aligned} & \int_V C_{ijkl} \Delta \varepsilon_{kl} \delta \varepsilon_{ij} dV - \int_{S^c} \frac{\partial T_i}{\partial w_j} \Delta w_j \delta w_i dS \\ & = \int_{S^c} T_i^t \delta w_i dS + \int_V b_i^{t+\Delta t} \delta u_i dV + \int_{S^x} t_i^{t+\Delta t} \delta u_i dS \\ & - \int_V \left[\sigma_{ij}^t - C_{ijkl} (\Delta \varepsilon_{kl}^{th} + \Delta \varepsilon_{kl}^{hy} + \Delta \varepsilon_{kl}^{pl} + \Delta \varepsilon_{kl}^{cr}) \right] \delta \varepsilon_{ij} dV. \end{aligned} \quad (33)$$

The last term on the right-hand side of Eq. (33) contains $\Delta \varepsilon_{kl}^{hy}$, $\Delta \varepsilon_{kl}^{pl}$ and $\Delta \varepsilon_{kl}^{cr}$, which depend on stress; see Section 2.5. Here, these strain increments will be evaluated using $\sigma_{ij}^{t+\Delta t}$, i.e. the unknown stress state at the end of the time step. Hence, Eq. (33) will be solved iteratively by use of fully implicit (backward Euler) time stepping.

3.2.2. Discretization with respect to space

The spatial discretization of Eq. (33) is based on a finite element formulation with continuum (volume) elements and cohesive (surface) elements. The former obey the material constitutive relation in Eq. (13), while the latter embed the decohesion law described in Appendix B. Our formulation is restricted to the case of small strains and small deformations [33]. Starting with the continuum elements, we express the spatial variation of the unknown displacement increments Δu_i within each element by interpolation in the element nodal values, Δu_i^q . More exactly, we consider Eq. (33) within a continuum finite element with volume V_e , and apply Eq. (25) for representing Δu_i , δu_i and their associated strains, $\Delta \varepsilon_{ij} = (\Delta u_{ij} + \Delta u_{ji})/2$ and $\delta \varepsilon_{ij} = (\delta u_{ij} + \delta u_{ji})/2$, within the element. This results in a system of linear equations for the displacement increments in the element nodes

$$\sum_{q=1}^N \mathcal{K}_{ij}^{pq} \Delta u_j^q = \mathcal{F}_i^p - \mathcal{Q}_i^p, \quad (34)$$

where N is the number of nodes in the element. The system matrix for continuum elements in Eq. (34) is defined through

$$\mathcal{K}_{ij}^{pq} = \int_{V_e} B_{klip} C_{klmn} B_{mnjq} dV, \quad \text{where} \quad (35)$$

$$B_{klip} = \frac{1}{2} (H_{p,l} \delta_{ik} + H_{p,k} \delta_{il}).$$

In Eq. (35), indices p and q refer to element node numbers, whereas indices i to n refer to spatial directions. Hence, for a continuum element with N nodes, the system matrix \mathcal{K}_{ij}^{pq} will be of size $3N \times 3N$ for a three-dimensional problem. We note that \mathcal{K}_{ij}^{pq} is symmetric.

The first term on the right-hand side of Eq. (34) contains body forces and external surface tractions, condensed to element nodal forces through

$$\mathcal{F}_i^p = \int_{V_e} b_i^{t+\Delta t} H_p dV + \int_{S_e^x} t_i^{t+\Delta t} H_p dS, \quad (36)$$

where S_e^x is the element's contribution to the external surface S^x . The second term comprises equivalent internal forces, defined by

$$\mathcal{Q}_i^p = \int_{V_e} B_{klip} [\sigma_{kl}^t - C_{klmn} (\Delta \varepsilon_{mn}^{th} + \Delta \varepsilon_{mn}^{hy} + \Delta \varepsilon_{mn}^{pl} + \Delta \varepsilon_{mn}^{cr})] dV. \quad (37)$$

Next, we consider a cohesive surface element, as illustrated in Fig. 6. The element consists of two surfaces, S_e^+ and S_e^- , which are made up of continuum elements at opposite sides of the potential crack path. A local coordinate system, (x'_1, x'_2, x'_3) , is defined such that the x'_3 -axis constitutes a normal to the crack surface, pointing towards S_e^+ .

Within the element, the local displacement jumps w_i across the crack surface are calculated by interpolation in the element nodal displacements u_i^q by use of a specific set of shape functions, \tilde{H}_q

$$w_i(\vec{r}, t) = \sum_{q=1}^N \tilde{H}_q(\vec{r}) u_i^q(t). \quad (38)$$

The shape functions \tilde{H}_q are compatible with those used in the continuum elements aside of the crack surface, but \tilde{H}_q at the lower (negative) side have opposite sign. Hence, for the 8-noded surface element in Fig. 6, $\tilde{H}_{q+4} = -\tilde{H}_q$, where $q = 1, \dots, 4$. This particular element is used for joining 8-noded (brick) continuum elements at opposite sides of the crack surface. For other types of continuum elements, compatible cohesive surface elements are easily constructed in the same manner.

Combining Eqs. (33) and (38), we get the equations for mechanical equilibrium within the cohesive surface element

$$\sum_{q=1}^N \mathcal{K}_{ij}^{pq} \Delta u_j^q = -\mathcal{Q}_i^p, \quad (39)$$

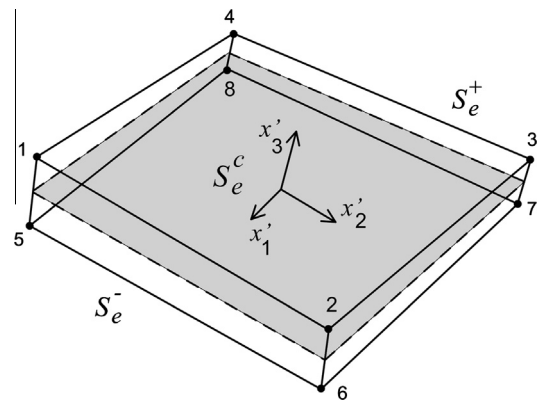


Fig. 6. Illustration of a cohesive surface element, which is used for joining continuum elements at opposite sides (S_e^+ and S_e^-) of the potential crack path (shaded) through the structure. The number of nodes and the shape functions are chosen such that the cohesive surface elements are compatible with the adjoining continuum elements.

where the element system matrix and the equivalent internal forces are defined by

$$\mathcal{K}_{ij}^{pq} = \int_{S_e^c} \frac{\partial \mathcal{T}_i}{\partial w_j} \tilde{H}_p \tilde{H}_q dS, \quad (40a)$$

$$\mathcal{Q}_i^p = \int_{S_e^c} \mathcal{T}_i^t \tilde{H}_p dS. \quad (40b)$$

These expressions are valid for a general decohesion law $\mathcal{T}_i(w_j)$.

The integrals in Eqs. (35)–(37) and Eq. (40) are evaluated by recourse to numerical quadrature, using standard methods for isoparametric finite elements [33]. The element contributions are assembled into a global system of linear equations for the unknown nodal increments of u_i . Since the element system matrices in Eqs. (35) and (40) are symmetric, the global system also becomes symmetric, which eases the numerical solution. However, iterations are needed in most time steps, since the constitutive relation used for the continuum, and also the decohesion law used for fracture modelling, are nonlinear.

4. Validation of the model

We have verified the correctness of the numerically implemented model by comparing calculated results with analytical solutions to simple benchmark problems for hydrogen diffusion and metal-hydride phase transformation. Also, we have validated the model against experiments reported in open literature. In the following, we consider five of these experiments, which were done to study hydrogen transport, metal-hydride phase transformation and stress-directed orientation of δ -hydrides in zirconium alloys. Zirconium alloys are considered in the examples, since experimental data are more abundant for these materials than for other metals that form binary hydrides, such as titanium or hafnium.

The material properties applied in our calculations are defined in Table 1. As indicated in the table, most of the data are taken from literature sources and pertain to the Zircaloy-2 (Zr–1.50Sn–0.15Fe–0.10Cr–0.120–0.05Ni by wt%) and Zircaloy-4

(Zr–1.50Sn–0.20Fe–0.11Cr–0.130 by wt%) alloys, which are used in cladding tubes of light water reactor nuclear fuel rods [3]. For the non-elastic deformation of the material, we use a model for combined viscoplasticity and creep, which considers the anisotropy of the material [35].

The experiments treated in the following subsections are fairly simple, but still, they address many important phenomena and are therefore suited for model validation. In Part II [6], the model is validated against experiments on fracture of hydrided zirconium alloys.

4.1. Hydrogen redistribution in a compositional gradient

Simple, yet telling, experiments on hydrogen redistribution under isothermal and stress-free conditions were carried out by Kammenzind and co-workers [45]. Rectangular samples ($25.4 \times 12.7 \times 0.96$ mm) of Zircaloy-4 sheet material were pre-charged with various amounts of hydrogen to produce diffusion couples, meaning that opposite ends of the samples were charged to different pretest concentrations of hydrogen. The hydrogen charging was done electrolytically, which created a sharp concentration gradient at the middle of each sample. After hydrogen charging, the diffusion couples were isothermally annealed at 633 K for 100 days. The annealing temperature was uniform across the samples, and no mechanical load was applied. After cooling, the samples were destructively analysed to quantify the hydrogen redistribution that had occurred during the anneal [45].

Fig. 7 shows the pre- and posttest distributions of hydrogen in one of the tested samples, which was precharged with hydrogen to concentrations of 10 wppm (left half, $z < 12.7$ mm) and 435 wppm (right half, $z > 12.7$ mm). The posttest measurements clearly show that the hydrogen concentration in the left half of the sample increased to about 135 wppm, which corresponds to the hydrogen terminal solid solubility under dissolution (TSSD) in Zircaloy-4 at 633 K; see C_L^{TSSD} in Table 1. The redistributed hydrogen originates from the right half of the diffusion couple, where a region close to the centre of the sample obviously lost much of its initial hydrogen content.

Fig. 7 also includes the results from a simulation of the test with our computational model. The calculations were done with a two-dimensional model of the sample, consisting of 50×25 8-noded quadrilateral finite elements of equal size. All material properties

Table 1

Material properties used in calculations. The material properties are for Zircaloy metal and zirconium δ -hydride (ZrH_{1.66}), as indicated with superscript m and h, respectively. E and ν are the Young modulus and Poisson ratio of the material. The temperature, T , is in kelvin.

	Source
Hydrogen transport properties	
$D^m(T) = 7.730 \times 10^{-7} \exp(-5450.4/T) \text{ m}^2 \text{ s}^{-1}$	[36]
$D^h(T) = 1.095 \times 10^{-7} \exp(-7798.6/T) \text{ m}^2 \text{ s}^{-1}$	[37]
$Q^m = 25,000 \text{ J mol}^{-1}$	[38,39]
$Q^h = 5400 \text{ J mol}^{-1}$	[40]
$V^m = V^h = 1.67 \times 10^{-6} \text{ m}^3 \text{ mol}^{-1}$	[32,41]
$c = C_s^h/C_s^m = 0.05$	This work
$A_{kl} = K\delta_{kl}$	This work
Metal-hydride phase transformation properties	
$C_L^{\text{TSSD}}(T) = 1.43 \times 10^5 \exp(-4413/T) \text{ wppm}$	[42]
$C_L^{\text{TSSP}}(T) = 3.27 \times 10^4 \exp(-3012/T) \text{ wppm}$	[42]
$C_U = 97,300 \text{ mol m}^{-3}$	[19]
$\Omega(\kappa) = \tanh(62.5\kappa)$	This work
$l_s = 3.0 \times 10^{-5} \text{ m}$	This work
$\gamma_c^h = 1.38 \times 10^{-26} \text{ m}^3$	This work
$(\eta_{0r}, \eta_{0\phi}, \eta_{0z}) = (0.98, 0.01, 0.01)$	This work
Mechanical deformation properties	
$E(T) = 1.028 \times 10^{11} - 5.475 \times 10^7 T \text{ Pa}$	[43]
$\nu = 0.45$	[43]
$\alpha^m = 6.50 \times 10^{-6} \text{ K}^{-1}$	[43]
$\alpha^h = 1.42 \times 10^{-5} \text{ K}^{-1}$	[1,44]
$\bar{V}^{\text{Hm}} = 1.67 \times 10^{-6} \text{ m}^3 \text{ mol}^{-1}$	[32,41]

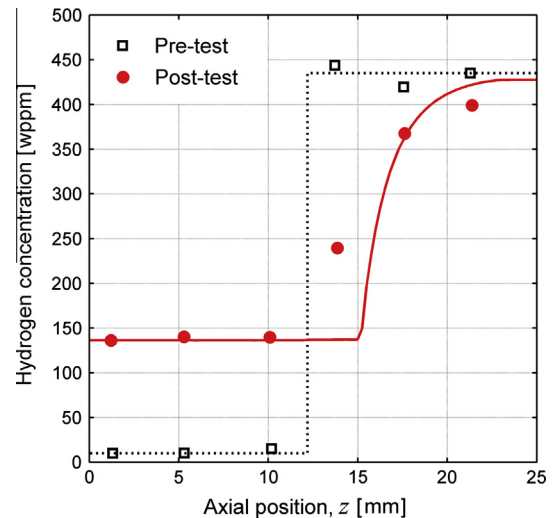


Fig. 7. Measured (markers) and calculated (lines) hydrogen distributions in an isothermal diffusion test on Zircaloy-4 material [45]. The posttest distribution results from isothermal annealing at 633 K for 100 days.

used in the calculations are defined in Table 1. The calculated posttest distribution of hydrogen is in fair agreement with the measured distribution: It should be remarked that the measurements were done by sectioning the sample into no more than six equal-size pieces, which were analysed for hydrogen by hot extraction [45]. Hence, the data points in Fig. 7 represent average hydrogen concentrations for fairly large volumes of material, and the exact shape of the steep concentration gradient is therefore unknown.

In this experiment, the redistribution of hydrogen takes place by diffusion of free hydrogen to the low-concentration half of the sample, and continues until the concentration of hydrogen in solid solution, C_s , becomes uniform and equal to the TSSD throughout the sample. This is illustrated in Fig. 8, which shows the calculated space–time evolution of C_s . In the high-concentration half of the sample, C_s is maintained at TSSD by continuous dissolution of hydrides as the hydrogen in solid solution diffuses into the low-concentration region to the left. The diffusion rate decreases as C_s approaches TSSD throughout the sample.

We note that Kammenzind et al. [45] failed to reproduce the experimental results in Fig. 7 with a computational model based on the early work of Marino [46]. They speculated that the disagreement between their calculated and measured results was due to the fact that their model considered hydride dissolution as an instantaneous process, and claimed that the data indicated that the dissolution was actually sluggish [45]. We have tested this hypothesis by repeating our simulation of the experiment, using different values for τ_d , the characteristic time for hydride dissolution, as defined by Eqs. (7) and (8) in Section 2.3. More exactly, we used l_s in the range from 10 to 250 μm , which at a temperature of 633 K gives τ_d from about 0.7 to 440 s. The calculated posttest hydrogen distribution was practically unaffected by τ_d over this range, which suggests that hydride dissolution in the experiment was sufficiently fast not to affect the outcome of the test. Hence, the hypothesis by Kammenzind et al. [45] seems to be incorrect, and the failure of their model to reproduce the test could have other reasons.

4.2. Hydrogen redistribution at a material interface

Hydrogen may redistribute at material interfaces, if there are differences in hydrogen solubility between the neighbouring mate-

rials. This phenomenon is of practical importance for e.g. welds and surface coatings (liners) in hydride forming metals. As an example, we will simulate the illustrative experiment by Takagi and co-workers [47,48], who studied the radial redistribution of deuterium in zirconium-lined Zircaloy-2 cladding tubes of light water reactor nuclear fuel rods. The tubes, which had an outer diameter of 12.27 mm, were manufactured with a 100 μm inside liner layer of almost pure zirconium: The liner is intended to protect the tubes against stress corrosion cracking by iodine and other aggressive fission products, released from the encapsulated nuclear fuel. The remaining part of the 860 μm thick tube wall consisted of Zircaloy-2. The terminal solid solubility of hydrogen and deuterium is slightly lower in the zirconium liner than in the Zircaloy-2 base metal. Here, we will make use of the correlations reported in [49]

$$C_L^{\text{TSSD}} = 1.41 \times 10^5 \exp(-4583/T), \quad (41a)$$

$$C_L^{\text{TSSP}} = 3.39 \times 10^4 \exp(-3282/T), \quad (41b)$$

where C_L^{TSSD} and C_L^{TSSP} is the hydrogen terminal solid solubility (wppm hydrogen) in the liner material under hydride dissolution and precipitation, respectively.

In each test, a 10 mm long section of the cladding tube was placed in a quartz tube filled with a certain amount of deuterium gas and heated to 673 K. The sample was held at this temperature for about 30 h, allowing the deuterium to enter the metal and to distribute uniformly through the sample. Then, the sample was slowly cooled from 673 to 433 K with a constant and controlled cooling rate, and subsequently cooled in air to room temperature. After the test, the radial distribution of deuterium across the tube wall was measured by nuclear reaction analysis; details of the methodology are given in [47].

In Fig. 9, we reproduce the measured posttest distribution of deuterium in one of the samples studied in [48]. This particular sample was charged with 0.88 atomic percent deuterium and cooled from 673 to 433 K at a rate of 1 K/min. It is clear that deuterium has moved from the Zircaloy-2 side to the zirconium side of the interface during the slow cooling.

In Fig. 9, we have included the results from numerical simulations of the experiment. In the simulations, we assumed a uniform distribution of 0.88 at% hydrogen in solid solution before the test, and calculated the hydrogen redistribution during cooling with a two-dimensional model of the cladding tube wall, consisting of

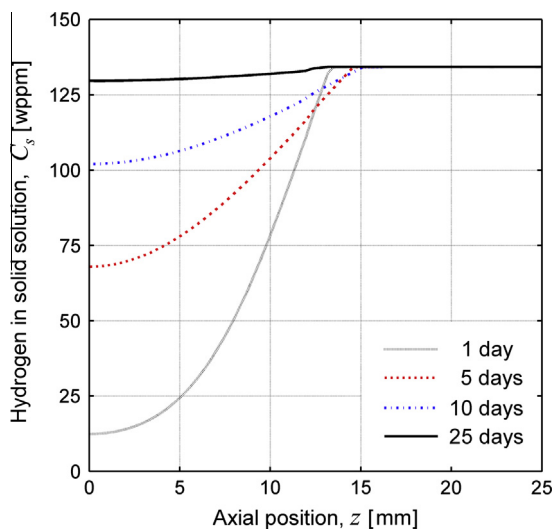


Fig. 8. Calculated space–time variation of free hydrogen concentration during the isothermal diffusion test in Fig. 7. The concentration approaches the TSSD (136 wppm) throughout the sample.

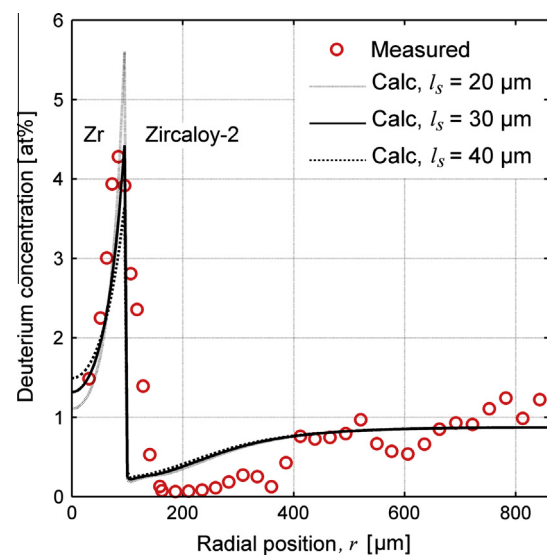


Fig. 9. Measured (circles) and calculated (lines) posttest distribution of deuterium in one of the liner cladding samples tested in [48]. The interface between the Zr liner and the Zircaloy-2 base material is at $r = 100 \mu\text{m}$.

86 8-noded quadrilateral finite elements of equal size across the cladding tube. The calculations were thus carried out for natural hydrogen (protium with 0.015 at% deuterium), and possible differences in solubility, diffusivity etc. between hydrogen and deuterium were neglected. All material properties used in the calculations are defined in Table 1, except for the terminal solid solubilities of hydrogen in the zirconium liner, which are defined in Eq. (41). Calculations were carried out for three different values of the typical length for hydrogen diffusion in the phase transformation process, l_s . As explained in Section 2.3, this parameter affects the precipitation kinetics, and from Fig. 9, it is clear that l_s has an impact on how far the deuterium diffuses into the liner layer from the interface. Fast precipitation, caused by a short diffusion length l_s , results in hydride formation very close to the interface, while slower precipitation allows more deuterium in solid solution to diffuse deeper into the liner layer before hydrides precipitate.

Fig. 10 shows the calculated deuterium flux across the Zr/Zircaloy-2 interface, and also the calculated difference in free deuterium concentration, C_s , between the Zircaloy-2 and the Zr side of the interface. This difference, which is the driving force for the flux, arises when hydrides start to precipitate at a temperature around 560 K. When the sample is further cooled, the difference in C_s increases, and so does the deuterium flux. The flux reaches a peak value at around 530 K; at lower temperatures, the flux drops as a result of decreasing diffusivity for deuterium in the metal.

4.3. Hydrogen redistribution in a temperature gradient

Temperature gradients are responsible for hydrogen redistribution in many structural components of zirconium and titanium alloys [38,50]. As an illustration, we simulate an experiment by Sawatzky [38], in which cylinders of Zircaloy-2, charged with either hydrogen or deuterium, were held in a steep temperature gradient for several weeks. The cylinders, 25 mm long and 12 mm in diameter, were precharged with controlled amounts of hydrogen or deuterium gas and annealed at 1173 K for six hours to produce an initially uniform hydrogen distribution. They were then placed in a fixture that allowed the two ends of the cylinder to be held at constant and different temperatures [38]. After being held for several weeks in the temperature gradient, the cylinders were removed and cut into 1 mm thick discs. These were analysed for hydrogen by hot extraction, and the axial hydrogen distribution thus determined.

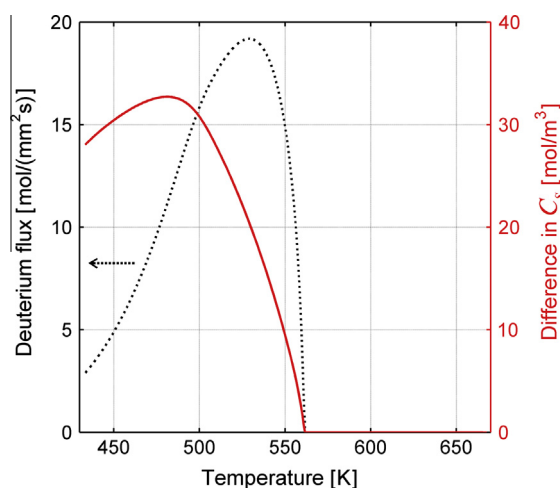


Fig. 10. Calculated deuterium flux (dashed line) across the Zr/Zircaloy-2 interface as a function of temperature during slow cooling from 673 to 433 K. The calculated difference in C_s (solid line) is evaluated as $C_s(r = 110 \mu\text{m}) - C_s(r = 90 \mu\text{m})$, where $r = 100 \mu\text{m}$ is the material interface position. The calculations were done with $l_s = 30 \mu\text{m}$.

Fig. 11 shows the posttest distribution of total hydrogen (hydrogen in solid solution and chemically bound in hydrides) for a sample with 130 wppm hydrogen, which was held at an average temperature gradient of 13.9 K/mm for 34 days; the hot and cold ends of the cylinder were held at 750 and 403 K. Also included in Fig. 11 are the results from two simulations of the test with our computational model.

The cylinder was modelled in two dimensions (axial symmetry) by use of fifty 8-noded elements of equal size, and a linear temperature variation along the cylinder was assumed. The material properties specified in Table 1 were used in the calculations, but for illustration, two alternative values for the hydrogen heat of transport in the Zircaloy-2 metal were applied.

Due to the thermal gradient, hydrogen in solid solution flows towards the cold end of the cylinder (Soret effect), at which a region with hydrided material is formed. Since the diffusivity of hydrogen is low at the cold end, the peak hydrogen concentration is reached at $z = 5\text{--}7 \text{ mm}$, where the temperature is 470–500 K. The hydrided region forms gradually, and the interface to the hydride-free part of the cylinder becomes increasingly sharper with time.

The calculated posttest distribution of hydrogen is in fair agreement with measurements. From Fig. 11, it is clear that the agreement is improved, when a higher value for Q^{m} than reported in the literature is used for the calculations. This does not imply that the higher value is correct, since there are other factors than Q^{m} that affect the calculated results. Most importantly, the calculations were done with an assumed linear temperature variation along the cylinder. The true temperature distribution may have been more complex, considering the small length-to-diameter ratio of the cylinder.

From Fig. 11, we also note that there is a small plateau in the calculated hydrogen distribution around $z = 10 \text{ mm}$. The plateau reflects the difference in hydrogen solid solubility during hydride precipitation and dissolution: Hydrides precipitate at the left (cold) end of the plateau, whereas they dissolve at the right (hot) end.

4.4. Hydrogen redistribution in a stress gradient

Next, we consider an experiment by Kammenzind and co-workers [45], in which stress-directed hydrogen diffusion was studied. Notched tensile specimens of Zircaloy-4, as shown in

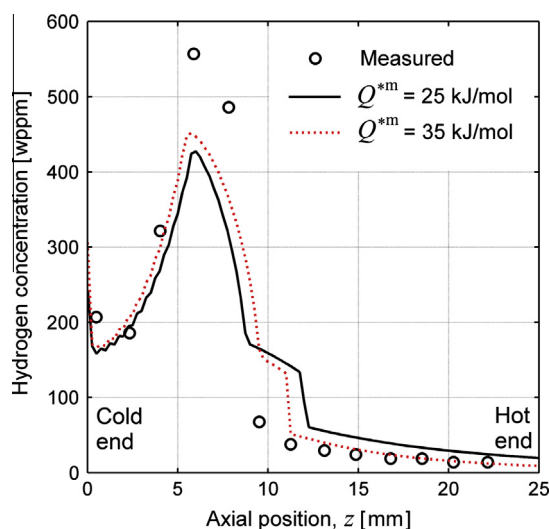


Fig. 11. Measured (circles) and calculated (lines) distribution of hydrogen in a Zircaloy-2 cylinder after a 34-day hold with cold/hot end temperatures of 403 and 750 K. The sample had a uniform initial distribution of 130 wppm hydrogen [38]. Calculations were done with two different values for the hydrogen heat of transport in the Zircaloy-2 metal, Q^{m} .

Fig. 12, were charged with hydrogen to a uniform concentration of about 330 wppm. Flat tensile specimens with overall dimensions $63.5 \times 20.3 \times 3.18$ mm were used, and a wide double-sided notch produced a stress concentration at the centreline of the sample. The specimens were subjected to constant dead-weight loading, concurrent with temperature cycling, for 20–50 days. The stress level, the peak temperature, and the number of thermal cycles were parametrically studied in a series of tests. After each test, the extent of hydrogen migration to the high-stress notch region was determined as the difference between the average concentration of hydrogen in the notched region and the average concentration far from the notch. These concentrations were measured by hot extraction of hydrogen from fairly large pieces of the specimen [45].

We have simulated two of the tests reported in [45]. The selected tests were carried out with a constant tensile stress in the notched region of either 160 or 240 MPa. The same temperature cycle was used in both tests: Each cycle lasted for 48 h and consisted of rapid heating to 644 K, a 46-h hold at that temperature, and slow cooling to below 320 K during the last two hours of the cycle. The extent of hydrogen redistribution was measured after 10 and 25 cycles, i.e. after 20 and 50 days.

A two-dimensional finite element model of the notched tensile specimen, as shown in Fig. 12, was used in all simulations. Since no information on the loading fixture design is given in [45], the remote parts of the specimen, containing holes for the loading fixture, were not considered in the finite element model. Instead, the loading applied in the model was that of a uniform boundary displacement, producing a constant tensile stress in the notched region of either 160 or 240 MPa; see Fig. 12. Plane strain deformation was assumed in the out-of-plane direction, and material properties used in the calculations are defined in Table 1.

Fig. 13a shows the calculated hydrogen distribution in the considered quarter of the specimen after 25 thermal cycles with a constant tensile stress in the notched region of 160 MPa. Hydrogen diffusion, driven by the gradient in hydrostatic pressure, has moved hydrogen from the low-stress region towards the end of the notched region. Hydrogen diffusion further into the notched

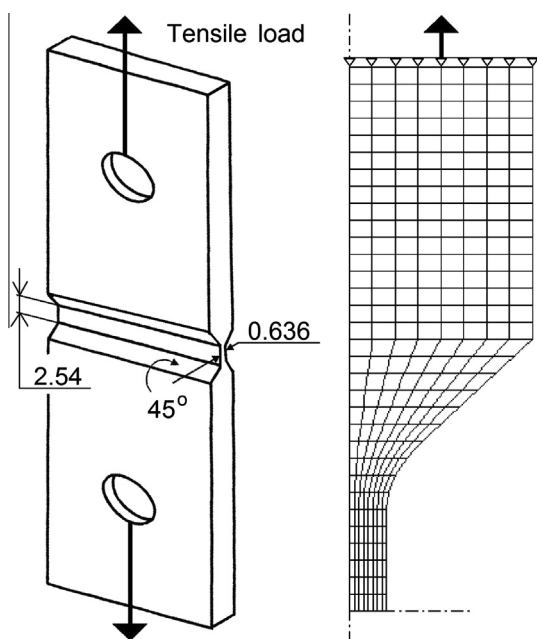


Fig. 12. Notched tensile specimen used in [45] (left) and two-dimensional finite element model of the specimen (right) applied in simulations. Thanks to symmetry, only a quarter of the specimen needs to be modelled.

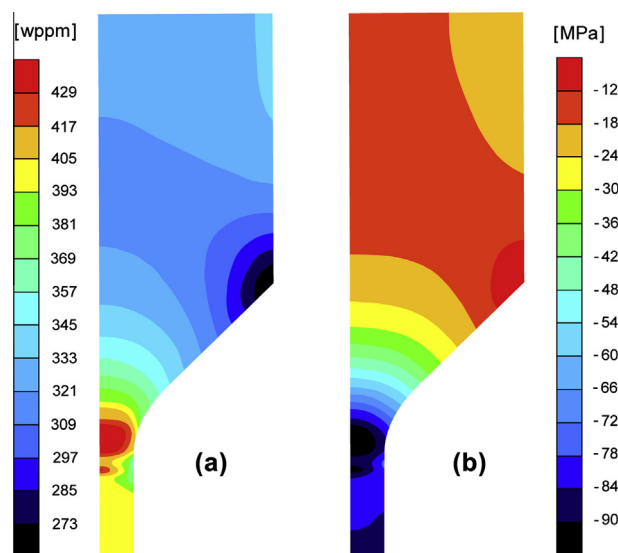


Fig. 13. Calculated distribution of (a) hydrogen after 25 thermal cycles and (b) hydrostatic pressure. The distributions are calculated for a test with a constant tensile stress of 160 MPa in the notched region.

region is driven by the concentration gradient alone, since the hydrostatic pressure is almost uniform within the notched region; see Fig. 13b. We note that Fig. 13a suggests that the peak hydrogen concentration is reached at the ends of the notched region, and consequently, that the *measured average* hydrogen concentration for the notched region will depend on whether the ends of the notch are included in the analysed sample or not; this is unclear for the measured data reported in [45].

Fig. 14 shows the calculated increase of hydrogen at the centre of the notched region, plotted as a function of time for two different stress levels. The calculated results are compared with the measured increase in *average* hydrogen concentration for the notched region, as reported in [45]. According to our calculations, the hydrogen concentration in the centre of the notched region increases by about 3 or 4 wppm (20 or 26 mol m⁻³) in each thermal cycle, depending on the stress level in the test. The overall result is a nearly linear increase in hydrogen concentration with time.

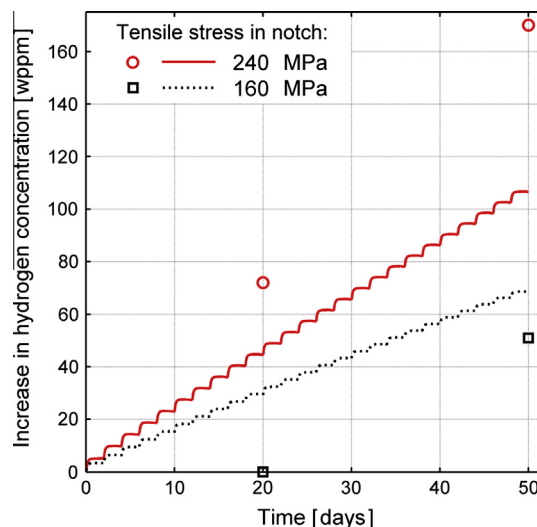


Fig. 14. Measured (markers) and calculated (lines) increase in hydrogen concentration for the notched region versus time. Results are shown for two different levels of constant tensile stress in the notched region [45].

It should be emphasized that the temperature cycling is essential for hydrogen transport in this test: If the temperature were held constant for 50 days, our calculations show that the total hydrogen increase would be no more than that observed for a single thermal cycle, i.e. either 3 or 4 wppm. The temperature cycling induces a ratchetting effect: During the hold at high temperature in each cycle, a gradient of hydrogen in solid solution is built up by the gradient in hydrostatic pressure. Since the gradient is weak, the high-end concentration of hydrogen in solid solution does not reach the TSSP, and hydrides are not formed directly at this stage. During the subsequent cooldown, however, most of the hydrogen is precipitated out as hydride, freezing it in place. When the sample is rapidly heated again, a uniform concentration of hydrogen in solid solution, equal to the TSSD, is obtained in the material. This initially uniform distribution is then gradually changed by stress-directed hydrogen diffusion during the high temperature hold, and the process repeats itself. Hence, in each thermal cycle, a small amount of hydrogen in solid solution is transported towards the high-stress region of the sample.

As shown in Fig. 14, the calculated results are in line with measured data. However, the model tends to overestimate the hydrogen transport at low stress, whereas the opposite is true at high stress. Possible reasons for these model-data differences are discussed in Section 5.3.

4.5. Stress-directed reorientation of hydrides

In Section 2.4, we showed that the state of stress during hydride precipitation affects the hydride orientation, which, in turn, affects the strength anisotropy of the material. Under operating conditions that involve temperature variations, one has to consider the possibility of stress-directed reorientation of existing hydrides. This phenomenon occurs when some part of the hydride population dissolves during heating, and then re-precipitates with a different orientation, dictated by the stress state under cooling. In case the heating and cooling cycle is repeated, a large part of the hydride population may ultimately be reoriented, even though only part of the population is dissolved in each temperature cycle. Hence, thermal cycling under stress may change the hydride orientation such that the material gradually loses its strength in the direction given by the dominating principal stress. This may ultimately lead to failure.

Here, we will simulate some experiments on stress-directed reorientation of hydrides during thermal cycling, carried out on Zircaloy-4 cladding tubes of light water reactor nuclear fuel rods by Chu and co-workers [10]. Short-length samples of the tubes, which had an outer diameter of 9.50 mm and a wall thickness of 0.58 mm, were precharged with hydrogen in stress-free condition. This produced a hydride population with almost exclusively “circumferential” hydrides, as shown in Fig. 2a. The tube samples were then loaded with a constant internal overpressure of 20.7 MPa and thermally cycled between 443 and 673 K in an autoclave. The nearly constant hoop stress in the samples, 150–160 MPa, changed the preferential plane for hydride precipitation from circumferential to radial, and the fraction of “radial” hydrides was measured after 1, 2, 4, 8 and 12 thermal cycles. The experimental details are described in [10].

Fig. 15 reproduces the results from three series of tests reported in [10], carried out on cladding tubes with 250, 320 and 600 wppm hydrogen. The fraction of radial hydrides, θ_ϕ , increased with the number of thermal cycles, and the increase was largest and fastest for the samples with the lowest hydrogen concentration (250 wppm). After 12 thermal cycles, more than 90% of the hydrides were radially aligned in the samples with 250 and 320 wppm hydrogen. The corresponding fraction for the 600 wppm samples was significantly lower.

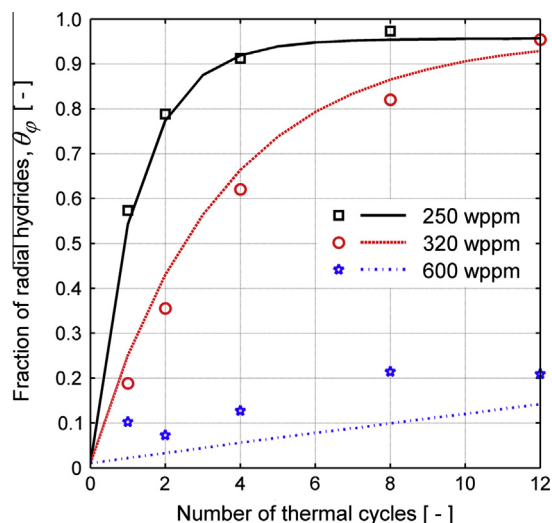


Fig. 15. Measured (markers) and calculated (lines) stress-directed reorientation of hydrides in Zircaloy-4 cladding tubes under thermal cycling. The hoop stress was held nearly constant at 150–160 MPa throughout the tests [10].

The hydride reorientation experiments by Chu and co-workers were simulated with our computational model, using the thermal-mechanical loading conditions detailed in [10]. The material properties used in the simulations are defined in Table 1. The pre-test hydride orientation in all samples was assumed to be ($\theta_r = 0.98, \theta_\phi = 0.01, \theta_z = 0.01$), i.e. 98% of the hydrides were assumed to be “circumferential” before the test. Calculated results for the evolution of θ_ϕ during thermal cycling are shown for samples with 250, 320 and 600 wppm hydrogen in Fig. 15. The overall agreement between the calculated results and the data is good, although the model slightly underestimates the fraction of reoriented hydrides for the samples with 600 wppm hydrogen. The results are further discussed in Section 5.3.

5. Discussion

5.1. Modelling approach

Over the years, computational models have been proposed for various aspects of hydrogen behaviour in hydride-forming metals. The models found in the literature are predominantly for zirconium and its alloys, and most of them are focussed on a single or a few phenomena, such as hydrogen transport or hydride induced embrittlement. Since the models are usually restricted to simple geometries and thermo-mechanical loading conditions, they rarely lend themselves to engineering applications, where concurrent and interacting phenomena must be considered in components that are subject to non-trivial histories of temperature and load.

Table 2 is a summary of computational models for the behaviour of hydrogen and hydrides in zirconium alloys, published in open literature. Our model is included in the table for comparison. As indicated in the table, the models can be divided into five categories: (i) Models for hydrogen diffusion and metal-hydride phase transformation in presence of temperature gradients. Mechanical aspects, including stress-directed hydrogen diffusion, are not modelled. (ii) Models for hydrogen diffusion and metal-hydride phase transformation in presence of stress gradients, assuming uniform temperature ($\nabla T = 0$). Feedback effects on the stress state from phase transformation (misfit strains) are considered. (iii) Cohesive zone models for fracture of hydrided materials with postulated hydride morphology and orientation, where neither hydrogen diffusion nor phase transformation is considered. (iv) Phase field

Table 2

Overview of computational models for the behaviour of hydrogen and hydrides in zirconium alloys. Here, ∇T and ∇p indicate the considered driving forces for hydrogen diffusion, and the value of τ defines if the time dependence of metal-hydride phase transformation is considered. “Yes” and “No” simply indicate whether the phenomenon is accounted for. The listed strains indicate the non-elastic deformation mechanisms considered in each model; see Section 2.5 for explanation. [†]The fracture model presented in [51,52] is restricted to constant velocity crack growth.

Category	Dimensions	Hydrogen transport	Phase transformation	Hydride orientation	Material deformation	Material fracture	Reference
(i)	2D	∇T	$\tau > 0$	No	No	No	[46]
	2D	∇T	$\tau > 0$	No	No	No	[53]
(ii)	3D	∇p	$\tau = 0$	No	$\varepsilon^{\text{pl}}, \varepsilon^{\text{hy}}$	No	[54]
	2D	∇p	$\tau = 0$	No	$\varepsilon^{\text{pl}}, \varepsilon^{\text{hy}}$	No	[55]
(iii)	2D	No	No	No	$\varepsilon^{\text{pl}}, \varepsilon^{\text{hy}}$	Yes	[56]
	3D	No	No	No	ε^{pl}	Yes	[57]
(iv)	2D	∇p	$\tau > 0$	Yes	ε^{hy}	No	[58]
	2D	∇p	$\tau > 0$	Yes	$\varepsilon^{\text{pl}}, \varepsilon^{\text{hy}}$	No	[59,60]
(v)	2D	$\nabla T, \nabla p$	$\tau = 0$	No	$\varepsilon^{\text{th}}, \varepsilon^{\text{hy}}$	Yes	[61,62]
	2D	∇p	$\tau = 0$	No	$\varepsilon^{\text{pl}}, \varepsilon^{\text{hy}}$	Yes [†]	[51,52]
	3D	$\nabla T, \nabla p$	$\tau > 0$	Yes	$\varepsilon^{\text{th}}, \varepsilon^{\text{pl}}, \varepsilon^{\text{cr}}, \varepsilon^{\text{hy}}$	Yes	Present work

models, by which the evolution of hydride morphology and orientation is calculated. (v) Integrated models, in which fracture is considered together with hydrogen diffusion and metal-hydride phase transformation.

It should be remarked that Table 2 is not a complete list of computational models that have been proposed for hydrogen and hydride behaviour in zirconium alloys over the years. The listed models are either seminal or have particular qualities that make them good examples for model categories (i)–(v). It is clear from Table 2 that our model stands out from most of the literature models, since it comprises a larger set of phenomenologically based sub-models. The sub-models are also in most cases more general than those used in other models listed in Table 2. This is further discussed in the following subsections.

5.1.1. Representation of hydrided material

Our model uses a continuum material description, in which precipitates of δ -hydride are represented by two local state variables: the hydride volume fraction, κ , and the hydride mean orientation, θ_i ; see Section 2.1. The continuum approach is used also in the majority of models listed in Table 2: The exceptions are the category (iii) and (iv) models, in which the hydride phase is considered by explicit modelling of the precipitate geometry and material properties.

Our model is unique among the continuum-based models in Table 2, since it is the only one that considers hydride orientation along with hydride concentration. This is important, since the hydride orientation causes a significant anisotropy in deformation, strength and fracture toughness of the hydrided material. As will be shown in Part II [6], the main reason for including θ_i as material state variables in our model is that fracture cannot always be accurately modelled, unless the hydride orientation is considered.

While our modelling approach caters for the effects of hydride volume fraction and orientation, it does not address issues associated with other morphology parameters, such as shape and size of the hydride precipitates. These issues can only be studied by explicit modelling of the precipitates as second phase particles in the metal. A few finite element studies of this kind on hydrided zirconium alloys are available in the literature [56,57]. These studies were aimed at determining the macroscopic strength and fracture toughness of materials, given their hydride morphology, hydride volume fraction and orientation. The latter properties were not calculated by the models, but given as input to represent the hydride structures typically observed in cladding tubes of light water reactor nuclear fuel rods [56,57]. An alternative approach, which to the best of our knowledge has not yet been tested, would be to calculate the hydride structure by use of phase field models,

see Section 5.1.4, and to use the results as input to the analyses of fracture.

5.1.2. Hydrogen transport

As described in Section 2.2, our model considers hydrogen transport by lattice diffusion in the metal as well as in the hydride phase. This is an improvement with respect to the models listed in Table 2, which, with one exception [53], consider hydrogen diffusion only in the metal phase. Hence, most models in the literature treat the hydride phase as impermeable to free hydrogen. This simplification may work well for small hydride concentrations, but it is inappropriate for modelling hydrogen diffusion when $\kappa \rightarrow 1$. Hydrogen diffusion in the hydride phase is in our model treated by making a rather artificial division of hydrogen in the hydride phase into either free or chemically bound hydrogen. It is also assumed that the free hydrogen concentration in the hydride phase can be related to that in the metal phase through the relation $C_s^{\text{h}} = cC_s^{\text{m}}$, where $c \in [0, 1]$ is a dimensionless model parameter. This assumption is based on equilibrium considerations at the metal-to-hydride interface: When the two phases are in equilibrium, the hydrogen chemical potential should be the same at each side of the interface. This implies that the hydrogen concentrations of the two phases are interrelated [16,53]. The upper boundary for c is not obvious, but follows from inspection of Eqs. (D.1) and (D.2) in Appendix D, which show that \vec{j} is aligned with $\nabla \kappa$ when $c > 1$. This implies that free hydrogen would flow uphill gradients of κ , which in certain cases could lead to spontaneous redistribution of all hydrogen to a very small region with high hydride volume fraction. This unstable behaviour is unphysical. On the other hand, when $c < 1$, free hydrogen flows downhill gradients of κ . In this case, the assumed difference in free hydrogen concentration between the metal and hydride phase tends to reduce the spatial variation of κ , which is in line with expectations. The model parameter c is expected to be temperature dependent, but there are currently no data from which it can be determined for zirconium alloys. The value used for c in our calculations (0.05) is somewhat arbitrary. However, parametric studies show that the value of c has a negligible effect on the calculated results presented in Section 4, since they pertain to cases with small volume fractions of hydride phase.

The effect of hydride precipitates on the hydrogen flux is catered for by the diagonal tensor A_{kl} , as defined by Eq. (3) in Section 2.2. Each diagonal element A_{kk} is the fraction of hydrides on the projected area perpendicular to the k :th direction, and thus depends on both κ and θ_i . This approach is a three-dimensional generalization of the early work by Shewmon [63], who proposed a similar model for uniaxial diffusion in a two-phase material. It

should be remarked, however, that the analyses presented in Section 4 were all carried out with $A_{kl} = \kappa \delta_{kl}$, meaning that all effects of hydride orientation on the hydrogen flux were neglected. Experiments on hydrogen diffusion in densely hydrided materials are needed to elucidate these effects, and to formulate adequate analytical expressions for A_{kl} in terms of both κ and θ_i .

Another distinctive feature of our model is that the hydrogen diffusion is driven by gradients in both temperature and hydrostatic stress. As indicated in Table 2, most of the other models treat gradients in *either* temperature *or* stress; only the model by Varias and Massih [61,62] accounts for both. From the results presented in Section 4, it is clear that hydrogen diffusion induced by temperature gradients is more substantial than that caused by gradients in stress for the considered zirconium alloys. The contributions are proportional to the heat of transport and volume of transport for the metal phase (Q^m and V^m), while the effects of these parameters for the hydride phase (Q^h and V^h) are negligible for the cases considered in Section 4. The reason is that the hydride volume fraction is low and that the hydrogen diffusivity is two orders of magnitude lower in the hydride phase than in the metal for the temperatures considered in the calculations. It should also be remarked that the volumes of transport for the two phases have been set equal to the partial molar volumes of hydrogen in the materials, based on theoretical considerations of the hydrogen chemical potential in stressed solids [64]. It has been pointed out that V^{*w} may in fact be somewhat lower than \bar{V}^{Hw} , and that a material damage dependence may exist [65].

Finally, we note that hydrogen transport by other mechanisms than lattice diffusion is neglected by all models in Table 2. The models are therefore not sufficient for cases in which hydrogen is also transported by means of dislocation sweeping [66]. This transport mechanism, which is connected with plasticity and creep, is further discussed in Section 5.3.

5.1.3. Metal-hydride phase transformation

Our model considers the time dependence of the metal-hydride phase transformation, and it also accounts for the observed hysteresis in hydrogen solubility between hydride dissolution and precipitation; see Eq. (8) in Section 2.3. This should be compared with the literature models in Table 2. Some of these account for the time dependence of the phase transformation, as indicated by $\tau > 0$ in Table 2, but most of them make use of time-independent equilibrium models ($\tau = 0$), meaning that $\kappa \equiv \kappa_e$.

Moreover, the literature models in Table 2 are focussed on hydride precipitation, which means that they are confined to conditions of constant temperature or cooling. Hence, the hysteresis in hydrogen solubility between hydride dissolution and precipitation is not considered in these models. This is a shortcoming, which implies that for instance the thermal ratchetting phenomenon described in Section 4.4 cannot be reproduced by the models. An attempt to model the hysteresis was made by Varias and Feng [51,52], who in their work assumed a stress dependence for the hydrogen solubility. This, in combination with an elasto-plastic constitutive law for the hydrided material, in some cases introduced a weak hysteresis in hydrogen solid solubility between hydride dissolution and precipitation, caused by irreversible plastic deformation. However, the hysteresis during a simple heating/cooling temperature cycle was *not* captured, since the expansion of the precipitates was assumed to be isotropic in their model and therefore did not cause plastic deformation of the continuum material. Moreover, the modelling approach in [51,52] contradicts the observation that hydrogen solid solubility in zirconium alloys is practically independent of stress [67].

The precipitation and dissolution rates of δ -hydride in titanium and zirconium alloys are controlled by hydrogen diffusion on the sub-grain level, i.e. by diffusion close to the interface between

the hydride precipitate and the metal [19]. Since this short-range diffusion is not explicitly modelled in our continuum description of the material, its effects on the phase transformation kinetics are considered by the point-kinetics model defined in Eq. (8). This equation is a first order approximation to the diffusion controlled phase transformation kinetics [68]. It is appropriate only for near-equilibrium conditions, i.e. for cases with slow temperature variations, where $|\kappa - \kappa_e|/\kappa_e \ll 1$. It is also restricted to moderately hydrided materials, since the characteristic time τ is calculated from the hydrogen diffusivity in the metal phase; see Eq. (7). There are two reasons for using this approximate model in our work: Firstly, the phase transformation model defined by Eq. (8) can easily be incorporated in an efficient numerical solution scheme, as described in Appendix C. Secondly, experimental data on the phase transformation kinetics of δ -hydride in titanium and zirconium alloys are not sufficient to support more advanced models. This is also the reason why we have set the characteristic time for hydride dissolution, τ_d , equal to that for precipitation, τ_p , in the calculations. To reveal possible differences between τ_d and τ_p , one has to experimentally quantify the kinetics of both hydride dissolution and precipitation for the same material. With one exception [25], such studies are as yet unavailable for zirconium alloys.

5.1.4. Stress-directed orientation of hydride precipitates

As explained in Sections 2.4 and Appendix A, we calculate the mean orientation of δ -hydride precipitates based on a theoretical model for stress-directed orientation of second phase nuclei, combined with our sub-model for metal-hydride phase transformation. The resulting model is fairly simple, and contains only a few material-dependent parameters (\mathcal{V}_c^h, n_{oi}) and an empirical function, $\Omega(\kappa)$, that can be easily determined through hydride reorientation experiments, such as [69,70]. The model in Section 2.4 has evolved from a simpler two-dimensional version [71].

By calculating the hydride mean orientation and making use of the results in the sub-models for material deformation and fracture, our model has an advantage over most literature models in Table 2. For those models in Table 2 that do not account for hydride orientation, the material deformation by metal-hydride misfit is by necessity assumed to be isotropic. Likewise, if fracture is considered in the models, it is assumed that the material's fracture properties are unaffected by hydride orientation. This assumption may work in a material with a fixed and uniform hydride orientation, but it is unfit for modelling fracture in cases where the hydride orientation changes over time and/or space.

The models listed in category (iv) of Table 2 are phase field models. The phase field approach is a method for describing microstructure formation in solids via temporal and spatial dependence of continuous (field) functions, generically referred to as order parameters [72,73]. The approach does not place *a priori* constraints on the possible transformation pathways, and hence, it has the potential to predict the evolution of complex microstructures for prescribed thermo-mechanical loading histories of the material. For applications to the kinetics of second-phase precipitation, such as hydride nucleation and growth, the method employs two sets of coupled basic equations; namely an equation for a non-conserved order parameter field, and another equation for the conserved concentration field. Both equations involve functional derivatives of the total free energy of the system under consideration. The total free energy is the sum of the microstructural, the chemical, the elastic and the interaction field free energies. The microstructural and the chemical free energies are in the form of the Ginzburg–Landau functionals, expressed in terms of the order parameter field and the concentration field, respectively; see e.g. [74].

Examples of phase field modelling of hydride forming metals are the works of Ma and colleagues [58,75,76], who studied the morphology of hydride precipitation under applied loads in zirconium. They used a phase field kinetic model, similar to the aforementioned approach, for an assumed elastic response of the zirconium material in a two-dimensional setting. In later works [59,60], the group extended the model to include also plastic deformation of the zirconium metal. Nevertheless, their analyses of the hydride precipitation phenomenon are qualitative, and the results are mostly presented in terms of calculated morphological micrographs. Furthermore, their plasticity model is rather simplistic and is an add-on approach, i.e. foreign to the framework of the phase field microstructural phenomenology. Here, it should be remarked that plastic deformation has been modelled using the phase field approach by other investigators [77–79], and so have cracks and fracture [80–82]. However, this kind of models for the mechanical behaviour of materials have not yet been integrated with microstructural models for precipitation of second phase in solids. The phase field approach thus seems to require significant development to be used in a computational model like ours. We also note that current phase field models are mostly restricted to two dimensions, since the computational cost for 3D simulations is high [81,82].

5.1.5. Material deformation

Our model is designed for considering a variety of deformation mechanisms, and consequently, it has a wider range of application than existing computational models. From Table 2, we note that models available in the literature usually consider only deformation by elasto-plasticity in combination with hydrogen induced expansion. The latter is treated as isotropic in the literature models, since neither the hydride orientation nor the anisotropy that it entails is modelled. Most of the literature models in Table 2 consider expansion both by precipitation of hydrides and by hydrogen in solid solution, but two of them [54,56] neglect the latter contribution.

In all models listed in Table 2, including ours, it is tacitly assumed that the elasto-plastic properties of the two-phase material do not change with increasing hydride content. Hence, the elastic coefficients, yield strength and strain hardening of the continuum are assumed to be independent of the hydride phase fraction. This assumption is justified for the elastic coefficients, since δ -phase hydride in zirconium and titanium has about the same elastic properties as the base metal [30,31]. Detailed finite element analyses of the two-phase material also confirm that the compositional dependence of the elastic coefficients for the homogenized continuum material can be neglected [83,84].

As for the yield strength of the hydrided material, most existing studies on hydrided zirconium alloys show that there is a slight and almost linear rise in yield strength with increasing hydride fraction, up to $\kappa \approx 0.10$ [85–88]. Tensile yield strength data for higher hydride fractions in zirconium alloys are unavailable, since the densely hydrided material breaks by brittle fracture during testing. The strain hardening of zirconium alloys is reported to decrease slightly with increasing hydride fraction [89,90] in the range for which data are available ($\kappa < 0.1$).

Finally, it should be remarked that the creep law used in our model takes no account of the hydride phase fraction. Experiments, carried out on zirconium alloys with low concentrations (<600 wppm) of hydrogen [91,92], indicate that the effects of hydrogen and hydrides on creep are weak for temperatures below 700 K.

5.1.6. Fracture

As explained in Section 2.6, fracture is modelled by embedding a decohesion law for the material within a specific kind of finite

elements. A similar approach was used in [61,62]. A distinctive feature of our fracture model is that the decohesion law may vary dramatically with both space and time, as the material's strength and toughness are changed by local precipitation or dissolution of brittle hydrides. The fracture model and its validation against experiments on initiation and growth of hydride induced cracks is discussed in Part II [6].

5.2. Numerical solution strategy

As shown in Fig. 5, the partial differential equations for hydrogen transport and mechanical equilibrium are solved separately (weak coupling). This has several advantages, in comparison with solving them simultaneously (strong coupling). Firstly, the separation of the two problems eases maintenance of the source code. Algorithms and models for either of the problems can be modified, with a minimal risk for unintentionally changing the solution procedure for the other problem. This is otherwise a generic problem in multi-physics codes, which are usually developed and maintained by experts from different and non-overlapping disciplines.

Secondly, the separation makes it easy to apply sub-stepping schemes, in which different time sub-step lengths are used for solving the two different sets of PDEs. This is useful, since in most practical problems, the allowable time step lengths differ considerably between the hydrogen transport problem and the mechanical problem. If the interaction between the two problems is weak, sub-stepping with separate step lengths is then very efficient. In this context, it should be remarked that the global time stepping shown in Fig. 5 is intended primarily to ensure consistency between the hydrogen and mechanical analyses. The global time step length thus depends on the extent of hydrogen-mechanical interaction.

Thirdly, separate solution modules for hydrogen transport and mechanical equilibrium paves the way for functional parallelisation of the computer code, since the two sets of PDEs can be solved in parallel on separate processors with a very limited amount of inter-processor communication. On single processor machines, the two sets of equations are solved in tandem, beginning in each global time step with the hydrogen transport problem.

Finally, we recall that the linear system of equations for mechanical equilibrium is symmetric, whereas the system for hydrogen transport is unsymmetric; see Section 3.1.2. With a finite element model in N_d spatial dimensions, containing N_n nodes, we are thus to solve a sparse symmetric system with $N_d \times N_n$ unknowns for the mechanical equilibrium, and a sparse unsymmetric system with N_n unknowns for the hydrogen transport. Solving these systems separately, taking advantage of the symmetry for the larger system, is in most cases less costly than solving the unsymmetric system with $(N_d + 1) \times N_n$ unknowns that would result from merging the two problems [93]. This saving in computational cost should be weighed against the cost for additional iterations, which are needed to ensure consistency when solving the systems separately, as shown in Fig. 5.

5.3. Results of model validation

Five different experiments on hydrogen behaviour in zirconium alloys, reported in the literature, were simulated with our computational model in Section 4. The experiments, which are part of a larger database used for validating our model, pertained to hydrogen transport, metal-hydride phase transformation, and stress-directed orientation of hydride precipitates. In general, the model reproduced the results of these experiments accurately. However, there were some differences between model and data for the experiment on stress directed hydrogen diffusion by Kammenzind and co-workers [45] in Section 4.4 that deserve discussion.

The results in Fig. 14 suggest that our model overestimates the hydrogen transport at low stress (160 MPa), but underestimates it at high stress (240 MPa). A possible reason to these differences is that the model considers hydrogen transport only by diffusion, whereas the tests may involve hydrogen transport also by dislocation sweeping: In a material deforming by creep and/or plasticity, it is known that hydrogen in solid solution may be swept through the crystal lattice by moving dislocations. Experiments have shown that the hydrogen flux caused by this mechanism can be several orders of magnitude larger than the flux arising from lattice diffusion, and simple models for the mechanism predict that the flux of hydrogen caused by moving dislocations is directly proportional to the non-elastic strain rate [66,94]. In this context, we note that the calculated effective creep strain in the notched region of the samples after 25 thermal cycles in the tests by Kammenzind et al. [45] is 3.3 and 16.7% for the 160 and 240 MPa case, respectively. These calculated results suggest that creep deformation is sufficiently large to cause hydrogen transport by dislocation sweeping, and that the sweeping is expected to be $16.7/3.3 \approx 5$ times stronger for the high-stress test. Hence, a likely explanation for the model-data differences in Fig. 14 is that hydrogen transport by dislocation sweeping into the notched region is significant for the high stress test, but not considered by our computational model.

A comment should also be made on the comparison of our hydride orientation model with the experiments by Chu et al. [10] in Section 4.5. These experiments show that partial reorientation of a hydride population is possible by dissolution and subsequent reprecipitation of only a fraction of the hydrides. They also show that, by repeating the dissolution-precipitation cycle, the fraction of reoriented hydrides increases with each cycle. However, the sensitivity to thermal cycling depends strongly on the fraction of hydrides dissolved in each cycle; see Fig. 15. For the samples with 320 and 600 wppm hydrogen in Fig. 15, respectively 63 and 34% of the room temperature hydride content is dissolved at the peak cycle temperature of 673 K. As a consequence, the hydride orientation is much less affected by thermal cycling in the samples with 600 wppm hydrogen: The thermal cycling in this case merely makes existing hydrides shrink and grow, and there is very little nucleation of new hydrides in each cycle. This behaviour is fairly well captured by our hydride orientation model from Section 2.4, where a key element is the empirical function $\Omega(\kappa)$ in Eq. (9). As described in Section 2.4, this function defines the relative importance of hydride growth to hydride nucleation during an increase in hydride volume fraction. In calculations, we have used $\Omega(\kappa) = \tanh(62.5\kappa)$. This function satisfies the boundary conditions $\Omega(0) = 0$ and $\Omega(1) = 1$, and contains a single coefficient that has been fitted to the data presented in [10]. We believe that the hydride orientation model can be improved by using a more elaborate empirical relation for $\Omega(\kappa)$, properly calibrated against a larger database. It should be remarked that an earlier version of the model [71], in which $\Omega(\kappa) \equiv 0$, was unable to accurately reproduce the thermal cycling experiments by Chu and colleagues [10].

6. Conclusions

A computational model for hydrogen transport, hydrogen induced deformation, hydride induced embrittlement and fracture in metals that form binary hydrides, such as Zr and Ti, was presented. Sub-models for five fundamental phenomena in these metals were merged into a three-dimensional computational framework, in which the governing multi-field partial differential equations for the interacting phenomena are solved in an integrated manner by use of the finite element method. The considered phenomena are stress- and temperature-directed hydrogen diffusion, metal-hydride phase transformation, stress-directed

orientation of hydride precipitates, expansion of the material by interstitial hydrogen as well as hydride precipitates, and hydride induced fracture of the material. The result is a flexible computational model, which can be used to study a wide range of problems involving temperature- and/or stress-directed diffusion of hydrogen in combination with hydride precipitation and hydride induced fracture. The model is suited for engineering applications, since structures with arbitrary geometry and thermo-mechanical loading conditions can be modelled.

In this first part of our two-part paper, the applicability of the model was demonstrated by simulating five independent experiments on hydrogen transport, metal-hydride phase transformation and stress-directed hydride orientation in zirconium alloys. The calculated results agreed with the results of these experiments, and we conclude that the model has the capacity to reproduce metal-hydride phase transformation in combination with hydrogen diffusion driven by gradients in hydrogen concentration, temperature, stress and material properties. We also conclude that hydrogen diffusion induced by temperature gradients is more substantial than that caused by gradients in stress for the considered zirconium alloys. The most significant differences between calculated results and experimental data were found for stress-directed hydrogen transport under high stress. A possible reason to these differences is that the model considers hydrogen transport only by diffusion, whereas the high-stress tests, which resulted in significant creep deformation, may have involved hydrogen transport also by dislocation sweeping.

The experiments, as well as our computer simulations thereof, suggest that hydrogen transport in the considered zirconium alloys may be strongly affected by thermal cycling. The reason is that these alloys exhibit a significant hysteresis in hydrogen terminal solid solubility between heating and cooling. In cases where hydrides that precipitate during the low-temperature part of the thermal cycle are not completely dissolved during the high-temperature part, the hysteresis induces a ratchetting effect, whereby the hydrogen distribution may change by a small increment in each cycle. In components subjected to a large number of thermal cycles, the accumulated effect of these incremental changes may become significant, e.g. with respect to hydride embrittlement. Moreover, thermal cycling may also lead to gradual reorientation of hydrides in mechanically loaded components. Evaluations of hydride reorientation tests with thermal cycling, carried out on zirconium alloys, show that this phenomenon is captured by our computational model.

Although the experiments used for validation of our model are fairly simple, the results of the experiments are far from trivial, and they can hardly be understood or interpreted without computer modelling. However, our computational model is not intended primarily for simulating this kind of simple experiments: the true strength and novelty of the model lies in its integrated design and its capacity to model complex, real-world problems with concurrent and interacting phenomena, which may ultimately lead to failure of the component. The model's applicability to such problems is demonstrated in Part II of our paper [6], where the model is validated against experiments on initiation and growth of hydride induced cracks.

Finally, it should be reiterated that the model is not restricted to zirconium alloys, although the examples in this paper deal exclusively with such metals. With minor modifications, the model can be applied also to other group 4 metals (titanium and hafnium), which have similar metal-hydrogen phase systems. Application of the model to these metals requires no more than replacing the material properties defined for Zr alloys in Table 1 with the corresponding properties for the Ti or Hf alloy of interest. In principle, it would also be possible to extend the model from two phases (α -metal + δ -hydride) to three phases (α and β -metal

+ δ -hydride); see Fig. 1. However, calibration of the model against experimental data with three mixed phases would be challenging.

Acknowledgement

Financial support from the Swedish Foundation for Strategic Research (SSF) for L.O. Jernkvist is gratefully acknowledged.

Appendix A. Stress-directed hydride orientation

Hydrides nucleate in the direction that gives the minimal critical free energy of formation [28]. This direction depends on the material's grain structure and texture, but also on the applied stress, since hydride nucleation involves anisotropic straining of the material. A simple, yet useful, model for the stress-directed orientation can be derived from classical nucleation theory [95], which states that the number density of critical size hydride nuclei, \mathcal{N}_c , is given by the Boltzmann distribution

$$\mathcal{N}_c = \mathcal{N}_o \exp(-\mathcal{G}_c/k_B T), \quad (\text{A.1})$$

where \mathcal{G}_c is the Gibbs free energy for forming a critical size nucleus, and \mathcal{N}_o is the density of nucleation sites. Next, we partition \mathcal{G}_c into a part that is independent of applied stress, \mathcal{G}_{co} , and a stress interaction part [96]

$$\mathcal{G}_c = \mathcal{G}_{co} - \mathcal{V}_c^h e_{kl}^T \sigma_{kl}, \quad (\text{A.2})$$

where \mathcal{V}_c^h is the volume of the critical size hydride nucleus, and e_{kl}^T is the transformation (misfit) strain tensor related to hydride formation. Since e_{kl}^T is anisotropic, \mathcal{G}_c will depend on the orientation of the hydride nucleus with respect to the components of applied stress. Hence, consider a hydride nucleus oriented with its normal in the i :th coordinate direction. Let us denote the transformation strain tensor of a nucleus with this particular orientation e_{kl}^{Ti} . Then, the number density of critical size nuclei with this orientation, \mathcal{N}_{ci} , follows from Eqs. (A.1) and (A.2)

$$\mathcal{N}_{ci} = \mathcal{N}_{oi} \exp(-\mathcal{G}_{co}/k_B T) \exp(\mathcal{V}_c^h e_{kl}^{Ti} \sigma_{kl}/k_B T), \quad (\text{A.3})$$

where \mathcal{N}_{oi} is the density of nucleation sites for hydrides oriented in the i :th direction. The fraction of hydrides nucleated in the i :th direction, n_i , then follows from

$$n_i = \frac{\mathcal{N}_{ci}}{\sum_{j=1}^3 \mathcal{N}_{cj}} = \frac{n_{oi} \exp(\mathcal{V}_c^h e_{kl}^{Ti} \sigma_{kl}/k_B T)}{\sum_{j=1}^3 n_{oj} \exp(\mathcal{V}_c^h e_{kl}^{Tj} \sigma_{kl}/k_B T)}, \quad (\text{A.4})$$

where n_{oi} is the fraction of hydrides nucleated in the i :th direction under stress-free conditions. This is a material-dependent parameter, which can be determined through metallographic examinations of a specific material after hydride precipitation in stress-free conditions. Likewise, \mathcal{V}_c^h can be treated as a material-dependent fitting parameter.

The transformation strain tensor, e_{kl}^{Ti} , in Eq. (A.4) can be estimated from theory [97]. For example, the most common type of hydride in group 4 metals is the δ -hydride, which has a face-centered cubic structure [1,2]. The transformation strain tensor for δ -hydride can be approximated as transversally isotropic, i.e. it is defined by a strain ε_{\perp}^T in the normal direction of the hydride platelet, and a strain $\varepsilon_{\parallel}^T$ in directions perpendicular to the platelet normal. Neglecting all off-normal (shear) components of the transformation strain tensor for δ -hydride, it follows that

$$e_{kl}^{Ti} = \varepsilon_{\parallel}^T \delta_{kl} + (\varepsilon_{\perp}^T - \varepsilon_{\parallel}^T) \delta_{ik} \delta_{il}, \quad (\text{A.5})$$

which is the expression used in the model for δ -hydride (no summation over subscript i here). In zirconium alloys, $\varepsilon_{\perp}^T = 0.0720$ and $\varepsilon_{\parallel}^T = 0.0458$ [97]. Somewhat larger values (0.10 and 0.07) are reported for titanium [98].

Appendix B. Fracture

Consider a cohesive surface element as shown in Fig. 6, which embeds the decohesion law $\mathcal{T}'_i(w_j)$. Here, prime ($'$) means that the components refer to the local coordinate system (x'_1, x'_2, x'_3) , as defined in Fig. 6. We note that the x'_3 coordinate axis coincides with the crack surface normal. Following the approach in [99], we introduce an effective crack opening displacement, \hat{w} , defined by

$$\hat{w} = \sqrt{\beta^2 w_1^2 + \beta^2 w_2^2 + w_3^2} = \sqrt{E_{ij} w'_i w'_j}, \quad (\text{B.1})$$

where $E_{ij} = \beta^2 \delta_{ij} + (1 - \beta^2) \delta_{i3} \delta_{j3}$. The parameter $\beta \in [0, 1]$ assigns different weights to the sliding (shear) and normal (opening) displacement jumps across the crack plane; see Fig. 6. Here, we will consider a cohesive law that derives from a free energy potential Ψ through $\mathcal{T}'_i = \partial \Psi / \partial w'_i$. We also assume that the free energy potential Ψ depends on w'_j only through \hat{w} , which means that

$$\mathcal{T}'_i = \frac{\partial \Psi}{\partial w'_i} = \frac{\partial \Psi}{\partial \hat{w}} \frac{\partial \hat{w}}{\partial w'_i} = \frac{\partial \Psi}{\partial \hat{w}} \frac{1}{\hat{w}} E_{ij} w'_j = \frac{\hat{\mathcal{T}}(\hat{w})}{\hat{w}} E_{ij} w'_j. \quad (\text{B.2})$$

The scalar function $\hat{\mathcal{T}}(\hat{w}) = \partial \Psi / \partial \hat{w}$ in Eq. (B.2) represents the material's fracture behaviour, in similarity to a yield function for a deformation softening plastic material. It will be further described in Part II [6]. From Eq. (40), it is clear that the partial derivatives $\partial \mathcal{T}'_i / \partial w'_j$ are needed for evaluating the stiffness matrix of the cohesive surface elements. In local coordinates, we find from Eqs. (B.1) and (B.2)

$$\frac{\partial \mathcal{T}'_i}{\partial w'_j} = \frac{\hat{\mathcal{T}}}{\hat{w}} E_{ij} + \frac{1}{\hat{w}^2} \left(\frac{\partial \hat{\mathcal{T}}}{\partial \hat{w}} - \frac{\hat{\mathcal{T}}}{\hat{w}} \right) E_{ik} E_{jl} w'_k w'_l, \quad (\text{B.3})$$

which reveals that the stiffness matrix for the cohesive element is symmetric; see Eq. (40). Finally, we express Eqs. (B.2) and (B.3) with reference to the global coordinate system (x_1, x_2, x_3) through

$$\mathcal{T}_i = \mathcal{T}'_k R_{ki} \quad \text{and} \quad \frac{\partial \mathcal{T}_i}{\partial w_j} = \frac{\partial \mathcal{T}'_k}{\partial w'_l} R_{kl} R_{ij}, \quad (\text{B.4})$$

where R_{ij} defines the rotation of the local, crack-oriented, coordinate system with respect to the global coordinates through $x'_i = R_{ij} x_j$. If the finite element model is intended for analyses of structures with small deformations, rotations and strains, the orientation of the local coordinate system does not change significantly during the analysis. Hence, R_{ij} may be considered as constant, which simplifies the numerical implementation considerably.

Appendix C. Phase transformation

With the aim to formulate an efficient and fully implicit time stepping scheme for the hydrogen transport problem, we seek a linear relationship between $\Delta \kappa$ and $\Delta \kappa_s$, as defined by Eq. (20). For simplicity, we depart from the approximate (non-hysteresis) phase transformation model described by Eq. (5), with the aim to finally arrive at expressions for Y^I and Y^{II} valid for the general model in Eq. (8).

An exact solution from time t to $t + \Delta t$ can be found for Eq. (5), provided that τ is constant and κ_e varies linearly over the time step. Under these restrictions, the exact solution for $\Delta \kappa = \kappa^{t+\Delta t} - \kappa^t$ is

$$\Delta \kappa = \mathcal{E}(\kappa_e^t - \kappa^t - \dot{\kappa}_e \tau) + \dot{\kappa}_e \Delta t, \quad (\text{C.1})$$

where $\dot{\kappa}_e$ is the constant rate of change for κ_e and $\mathcal{E} = 1 - \exp(-\Delta t/\tau)$.

Next, we use Eq. (C.1) as an approximate solution to the general case, where τ and $\dot{\kappa}_e$ are no longer constant over Δt . We start by setting $\dot{\kappa}_e = \Delta \kappa_e / \Delta t$, where

$$\Delta\kappa_e = \frac{\partial\kappa_e}{\partial C_s} \Delta C_s + \frac{\partial\kappa_e}{\partial \kappa} \Delta\kappa + \frac{\partial\kappa_e}{\partial C_L} \Delta C_L + \mathcal{R}. \quad (\text{C.2})$$

Here, the partial derivatives of κ_e are calculated from Eqs. (2) and (6). \mathcal{R} is a residual, defined through

$$\mathcal{R} = \Delta\kappa_e^o - \frac{\partial\kappa_e}{\partial C_s} \Delta C_s^o - \frac{\partial\kappa_e}{\partial \kappa} \Delta\kappa^o - \frac{\partial\kappa_e}{\partial C_L} \Delta C_L^o, \quad (\text{C.3})$$

where superscript o refers to increments calculated in the previous iteration in the iterative solution sequence. By combining $\dot{\kappa}_e = \Delta\kappa_e/\Delta t$ with Eqs. (C.1) and (C.2), we find that

$$\Delta\kappa \left(1 - \mathcal{P} \frac{\partial\kappa_e}{\partial \kappa} \right) = \mathcal{P} \frac{\partial\kappa_e}{\partial C_s} \Delta C_s + \mathcal{E}(\kappa_e^t - \kappa^t) + \mathcal{P} \left(\frac{\partial\kappa_e}{\partial C_L} \Delta C_L + \mathcal{R} \right), \quad (\text{C.4})$$

where $\mathcal{P} = 1 - \mathcal{E}\tau/\Delta t$. Thus, when the approximate (non-hysteresis) phase transformation model in Eq. (5) is used, we may write $\Delta\kappa = Y^I \Delta C_s - Y^{II}$, where

$$Y^I = \left(1 - \mathcal{P} \frac{\partial\kappa_e}{\partial \kappa} \right)^{-1} \mathcal{P} \frac{\partial\kappa_e}{\partial C_s}, \quad (\text{C.5a})$$

$$Y^{II} = \left(1 - \mathcal{P} \frac{\partial\kappa_e}{\partial \kappa} \right)^{-1} \left[\mathcal{E}(\kappa^t - \kappa_e^t) - \mathcal{P} \left(\frac{\partial\kappa_e}{\partial C_L} \Delta C_L + \mathcal{R} \right) \right]. \quad (\text{C.5b})$$

The situation is slightly more complex when the phase transformation model with hysteresis, defined by Eq. (8), is used. In that case, we define separate phase equilibria for dissolution and precipitation, κ_d and κ_p , which replace κ_e in the above expressions. Hence, we calculate Y^I and Y^{II} for two scenarios, corresponding to dissolution and precipitation, respectively. If $\kappa^t > \kappa_d^{t+\Delta t}$, hydrides dissolve during the time step, and Y^I and Y^{II} should be calculated from Eq. (C.5) with $\kappa_e = \kappa_d$ and $\tau = \tau_d$. In contrast, if $\kappa^t < \kappa_p^{t+\Delta t}$, hydrides precipitate during the time step, and Y^I and Y^{II} should thus be calculated with $\kappa_e = \kappa_p$ and $\tau = \tau_p$. Finally, if $\kappa_p^{t+\Delta t} < \kappa^t < \kappa_d^{t+\Delta t}$, equilibrium conditions prevail, and $\Delta\kappa = 0$. In that case, $Y^I = Y^{II} = 0$.

Appendix D. Hydrogen transport

To efficiently solve the hydrogen transport equation, defined in Section 3.1.1, we need to express the unknown hydrogen flux at time $t + \Delta t$ as a linear combination of ΔC_s and $\Delta C_{s,k}$; see Eq. (21). Here, we derive analytical expressions for the functions X^I , X_k^{II} and X_k^{III} in Eq. (21), based on the constitutive relation in Eq. (4).

From Section 2.2, we know that $C_s = (1 - \kappa)C_s^m + \kappa C_s^h$ and that $C_s^h = cC_s^m$. Using these relations, we re-write the partial hydrogen fluxes in metal (m) and hydride (h) from Eq. (4) in terms of C_s . The results are:

$$J_k^m = -\frac{D^m}{\Theta} (C_{s,k} + C_s \Gamma_k^m), \quad (\text{D.1a})$$

$$J_k^h = -\frac{cD^h}{\Theta} (C_{s,k} + C_s \Gamma_k^h), \quad (\text{D.1b})$$

where the dimensionless denominator Θ is defined through $\Theta = 1 - \kappa(1 - c)$, and the driving forces for hydrogen diffusion, Γ_k^ω , are given by

$$\Gamma_k^\omega = \frac{Q^{*\omega}}{RT^2} T_{,k} + \frac{V^{*\omega}}{RT} p_{,k} + \frac{(1 - c)}{\Theta} \kappa_{,k}. \quad (\text{D.2})$$

As before, superscript ω in Eq. (D.2) is either m (metal) or h (hydride). It is interesting to note that, according to Eqs. (D.1) and (D.2), there will always be a hydrogen flux downhill gradients in κ , when $c < 1$.

Next, we combine Eqs. (D.1) and (D.2) with Eq. (3) from Section 2.2. In the latter equation, we also set $A_{kl} = \kappa \delta_{kl}$, meaning

that the effects of hydride orientation on the total hydrogen flux is neglected. The result can be written

$$J_k = -\left(W^m + W^h \right) C_{s,k} - \left(W^m \Gamma_k^m + W^h \Gamma_k^h \right) C_s, \quad (\text{D.3})$$

where $W^m = (1 - \kappa)D^m/\Theta$ and $W^h = c\kappa D^h/\Theta$.

Finally, we consider $J_k^{t+\Delta t}$, i.e. the components of the total hydrogen flux vector at the end of a time step from time t to $t + \Delta t$. As in Section 3.1.1, we decompose the concentration of hydrogen in solid solution at the advanced time $t + \Delta t$ into the already known quantity C_s^t at time t and an unknown increment ΔC_s ; see Eq. (17). With this decomposition inserted into Eq. (D.3), we get

$$J_k^{t+\Delta t} = -X^I \Delta C_{s,k} - X_k^{II} \Delta C_s - X_k^{III}, \quad (\text{D.4})$$

where $X^I = W^m + W^h$, $X_k^{II} = W^m \Gamma_k^m + W^h \Gamma_k^h$, and $X_k^{III} = X^I C_{s,k}^t + X_k^{II} C_s^t$. We note that all quantities in these expressions, except for C_s^t and $C_{s,k}^t$, should be evaluated at the advanced time $t + \Delta t$.

References

- [1] W.M. Mueller, J.P. Blackledge, G.G. Libowitz (Eds.), *Metal Hydrides*, Academic Press, New York, 1968.
- [2] C.E. Coleman, Cracking of hydride-forming metals and alloys, in: J. Petit, P.M. Scott (Eds.), *Environmentally Assisted Failure*, in: I. Milne, R.O. Ritchie, B. Karihaloo (Eds.), *Comprehensive Structural Integrity: Fracture of Materials from Nano to Macro*, vol. 6, Elsevier Pergamon, Amsterdam, 2003, pp. 103–161.
- [3] C. Lemaignan, A.T. Motta, in: R.W. Cahn, P. Haasen, E.J. Kramer (Eds.), *Nuclear Materials*, in: B.R.T. Frost (Vol. Ed.), vol. 10B of *Material Science and Technology*, VCH, Weinheim, 1994, pp. 1–51.
- [4] G. Lütjering, J.C. Williams, *Titanium*, Springer Verlag, Berlin, 2003.
- [5] F.D. Manchester (Ed.), *Phase Diagrams of Binary Hydrogen Alloys*, Monograph Series on Alloy Phase Diagrams, vol. 13, ASM International, Materials Park, 2000.
- [6] L.O. Jernkvist, *Comput. Mater. Sci.* 85 (2014) 383–401.
- [7] R.P. Marshall, M.R. Louthan, *Trans. ASM* 56 (1963) 693–700.
- [8] K.S. Chan, *Acta Metall. Mater.* 43 (1995) 4325–4335.
- [9] A.T. Motta, L.Q. Chen, *JOM* 64 (2012) 1403–1408.
- [10] H.C. Chu, S.K. Wu, K.F. Chien, R.C. Kuo, *J. Nucl. Mater.* 362 (2007) 93–103.
- [11] J.J. Kearns, J.C. Woods, *J. Nucl. Mater.* 20 (1966) 241–261.
- [12] J.B. Bai, C. Prioul, D. Francois, *Metall. Mater. Trans. A* 25A (1994) 1185–1197.
- [13] M. Veleza, S. Arsene, M.C. Record, J.L. Bechade, J.B. Bai, *Metall. Mater. Trans. A* 34A (2003) 567–578.
- [14] C.Q. Chen, S.X. Li, H. Zheng, L.B. Wang, K. Lu, *Acta Mater.* 52 (2004) 3697–3706.
- [15] M.I. Luppó, A. Politi, G. Vigna, *Acta Mater.* 53 (2005) 4987–4996.
- [16] P. Shewmon, *Diffusion in Solids*, second ed., The Minerals Metals and Materials Society (TMS), Warrendale, 1989.
- [17] M.E. Glicksman, *Diffusion in Solids*, John Wiley & Sons, New York, 2000.
- [18] J.L. Waisman, G. Sines, L.B. Robinson, *Metall. Trans.* 4 (1973) 291–302.
- [19] S. Banerjee, P. Mukhopadhyay, *Phase Transformations – Examples from Titanium and Zirconium Alloys*, Pergamon Materials Series, vol. 12, Elsevier, Amsterdam, 2007.
- [20] F.S. Ham, *J. Appl. Phys.* 30 (1959) 915–926.
- [21] J.J. Kearns, *J. Nucl. Mater.* 27 (1968) 64–72.
- [22] Y. Mishima, S. Ishino, S. Nakajima, *J. Nucl. Mater.* 27 (1968) 335–344.
- [23] K. Ue, S. Ishimoto, *J. Nucl. Mater.* 322 (2003) 66–72.
- [24] R. Tang, X. Yang, *Int. J. Hydrogen Energy* 34 (2009) 7269–7274.
- [25] O. Zanellato, M. Preuss, J.Y. Buffiere, F. Ribeiro, A. Steuwer, J. Desquines, J. Andrieux, B. Krebs, *J. Nucl. Mater.* 420 (2012) 537–547.
- [26] M.P. Puls, *Acta Metall.* 32 (1984) 1259–1269.
- [27] S. Qian, D.O. Northwood, *Int. J. Hydrogen Energy* 15 (1990) 649–654.
- [28] C.E. Ells, *J. Nucl. Mater.* 35 (1970) 306–315.
- [29] Y.C. Fung, *Foundations of Solid Mechanics*, Prentice Hall, Englewood Cliffs, 1965.
- [30] M.P. Puls, S.-Q. Shi, J. Rabier, *J. Nucl. Mater.* 336 (2005) 73–80.
- [31] O.N. Senkov, M. Dubois, J.J. Jonas, *Metall. Mater. Trans. A* 27A (1996) 3963–3970.
- [32] S.R. MacEwen, C.E. Coleman, C.E. Ells, J. Faber, *Acta Metall.* 33 (1985) 753–757.
- [33] K.J. Bathe, *Finite Element Procedures*, second ed., Prentice Hall, Englewood Cliffs, 1995.
- [34] J.A. Scott, *Commun. Numer. Methods Eng.* 22 (2006) 1015–1029.
- [35] L.O. Jernkvist, in: *Transactions of the 15th International Conference on Structural Mechanics in Reactor Technology (SMiRT 15)*, Seoul, Korea, vol. II, 1999, pp. 477–484 (Paper C04-3).
- [36] J.J. Kearns, *J. Nucl. Mater.* 43 (1972) 330–338.
- [37] H. Wipf, B. Kappesser, R. Werner, *J. Alloys Comp.* 310 (2000) 190–195.
- [38] A. Sawatzky, *J. Nucl. Mater.* 2 (1960) 321–328.
- [39] B.F. Kammenzind, D.G. Franklin, H.R. Peters, W.J. Duffin, in: E.R. Bradley, G.P. Sabol (Eds.), *Zirconium in the Nuclear Industry: Eleventh International*

- Symposium, ASTM STP 1295, American Society for Testing and Materials, 1996, pp. 338–370.
- [40] A.W. Sommer, W. Dennison, Thermal Diffusion of Hydrogen in Nonstoichiometric Zirconium-Dihydride, Technical Report NAA-SR-5066, Atomics International, Division of North American Aviation, Canoga Park, CA, USA, 1960.
 - [41] R.L. Eadie, K. Tashiro, D. Harrington, M. Leger, *Scripta Metall. Mater.* 26 (1992) 231–236.
 - [42] K. Une, S. Ishimoto, Y. Etoh, K. Ito, K. Ogata, T. Baba, K. Kamimura, Y. Kobayashi, *J. Nucl. Mater.* 389 (2009) 127–136.
 - [43] D.L. Hargman, G.A. Reymann, R.E. Mason, MATPRO-Version 11 (Revision 2) – A Handbook of Materials Properties for Use in the Analysis of Light Water Reactor Fuel Rod Behaviour, Technical Report NUREG/CR-0479, US Nuclear Regulatory Commission, Washington, DC, USA, 1981.
 - [44] G.B. Allen, M. Kerr, M.R. Daymond, *J. Nucl. Mater.* 430 (2012) 27–36.
 - [45] B.F. Kammenzind, B.M. Berquist, R. Bajaj, P.H. Kreyns, D.G. Franklin, in: G.P. Sabol, G.D. Moan (Eds.), *Zirconium in the Nuclear Industry: Twelfth International Symposium*, ASTM STP 1354, American Society for Testing and Materials, 2000, pp. 196–233.
 - [46] G.P. Marino, HYDIZ – A 2-Dimensional Computer Program for Migration of Interstitial Solutes of Finite Solubility in A Thermal Gradient, Technical Report WAPD-TM-1157, Bettis Atomic Power Laboratory, Pittsburgh, PA, USA, 1974.
 - [47] I. Takagi, T. Hattori, M. Hashizumi, K. Higashi, *Nucl. Instrum. Methods Phys. Res. B* 118 (1996) 238–241.
 - [48] I. Takagi, S. Shimada, D. Kawasaki, K. Higashi, *J. Nucl. Sci. Technol.* 39 (2002) 71–75.
 - [49] K. Une, S. Ishimoto, *J. Nucl. Sci. Technol.* 41 (2004) 949–952.
 - [50] R.P. Marshall, *Trans. Metall. Soc. AIME* 233 (1965) 1449–1450.
 - [51] A.G. Varias, J.L. Feng, *Comput. Mech.* 34 (2004) 339–356.
 - [52] A.G. Varias, J.L. Feng, *Comput. Mech.* 34 (2004) 357–376.
 - [53] J. Freund, A Model for Thermal Diffusion of Hydrogen in Zirconium Alloys, Technical Report PB93-122901, Institute of Mechanics, Helsinki University of Technology, Helsinki, Finland, 1992.
 - [54] D.R. Metzger, R.G. Sauvé, in: G.M. Hulbert (Ed.), *Computer Technology 1996: Applications and Technology*, ASME Pressure Vessels and Piping Conference, PVP-326, American Society of Mechanical Engineers, 1996, pp. 137–143.
 - [55] J. Lufano, P. Sofronis, *Comput. Model. Eng. Sci.* 1 (2000) 119–131.
 - [56] A.G. Varias, A.R. Massih, *Eng. Fract. Mech.* 65 (2000) 29–54.
 - [57] F. Perales, Y. Monerie, F. Dubois, L. Stainier, in: *Transactions of the 18th International Conference on Structural Mechanics in Reactor Technology (SMiRT 18)*, Beijing, China, 2005, pp. 274–280 (Paper B04-3).
 - [58] X.Q. Ma, S.Q. Shi, C.H. Woo, L.Q. Chen, *Mech. Mater.* 38 (2006) 3–10.
 - [59] X.H. Guo, S.Q. Shi, Q.M. Zhang, X.Q. Ma, *J. Nucl. Mater.* 378 (2008) 110–119.
 - [60] X.H. Guo, S.Q. Shi, Q.M. Zhang, X.Q. Ma, *J. Nucl. Mater.* 378 (2008) 120–125.
 - [61] A.G. Varias, A.R. Massih, *J. Nucl. Mater.* 279 (2000) 273–285.
 - [62] A.G. Varias, A.R. Massih, *J. Mech. Phys. Solids* 50 (2002) 1469–1510.
 - [63] P.G. Shewmon, *Trans. Metall. Soc. AIME* 212 (1958) 642–647.
 - [64] J.C.M. Li, R.A. Oriani, L.S. Darken, *Zeitschrift fuer Physikalische Chemie, Neue Folge* 49 (1966) 271–291.
 - [65] P.N. Adler, R.L. Schulte, E.J. Schneid, E.A. Kamykowski, F.J. Kuehne, *Metall. Trans. A* 11 (1980) 1617–1623.
 - [66] J. Tien, S. Nair, R. Jensen, in: I. Bernstein, A. Thompson (Eds.), *Hydrogen Effects in Metals: Proceedings of the Third International Conference on Effect of Hydrogen on Behavior of Materials*, TMS-AIME, Warrendale, 1981, pp. 37–56.
 - [67] S.Q. Shi, *Scripta Mater.* 41 (1999) 1115–1121.
 - [68] R.W. Balluffi, S.M. Allen, W.C. Carter, *Kinetics of Materials*, John Wiley & Sons, Hoboken, 2005.
 - [69] D. Hardie, M.W. Shanahan, *J. Nucl. Mater.* 55 (1975) 1–13.
 - [70] K. Sakamoto, M. Nakatsuka, *J. Nucl. Sci. Technol.* 43 (2006) 1136–1141.
 - [71] A.R. Massih, L.O. Jernkvist, *Comput. Mater. Sci.* 46 (2009) 1091–1097.
 - [72] A.G. Khachaturyan, *Theory of Structural Transformations in Solids*, Dover reprint 2008 ed., John Wiley & Sons, New York, 1983.
 - [73] R.C. Desai, R. Kapral, *Dynamics of Self-Organized and Self-Assembled Structures*, Cambridge University Press, Cambridge, 2009.
 - [74] P.C. Hohenberg, B.I. Halperin, *Rev. Mod. Phys.* 49 (1977) 435–479.
 - [75] X.Q. Ma, S.Q. Shi, C.H. Woo, L.Q. Chen, *Mater. Sci. Eng. A* A334 (2002) 6–10.
 - [76] X.Q. Ma, S.Q. Shi, C.H. Woo, L.Q. Chen, *Comput. Mater. Sci.* 23 (2002) 283–290.
 - [77] M. Koslowski, A. Cuitino, M. Ortiz, *J. Mech. Phys. Solids* 50 (2001) 2597–2635.
 - [78] M. Koslowski, *Philos. Mag.* 87 (2007) 1175–1184.
 - [79] M. Zaiser, *Adv. Phys.* 55 (2006) 185–245.
 - [80] L.O. Eastgate, J.P. Sethna, M. Rauscher, T. Cretegnny, C.S. Chen, C.R. Myers, *Phys. Rev. E* 65 (2002) 036117.
 - [81] Y. Wang, J. Li, *Acta Mater.* 58 (2010) 1212–1235.
 - [82] R. Spatschek, E. Brener, A. Karma, *Philos. Mag.* 91 (2011) 75–95.
 - [83] J.L. Feng, A.G. Varias, Y.K. Sui, *Int. J. Solids Struct.* 43 (2006) 2174–2192.
 - [84] P.G. Vincent, S. Bourgeois, Y. Monerie, *Mech. Mater.* 42 (2010) 175–188.
 - [85] J.H. Huang, S.P. Huang, *J. Nucl. Mater.* 208 (1994) 166–179.
 - [86] M. Grange, J. Besson, E. Andrieu, *Metall. Mater. Trans. A* 31A (2000) 679–690.
 - [87] S. Arsene, J.B. Bai, P. Bompard, *Metall. Mater. Trans. A* 34A (2003) 553–566.
 - [88] S.K. Yagnik, A. Hermann, R.C. Kuo, *J. ASTM Int.* 2 (2005) (Paper ID JAI12423).
 - [89] F. Yunchang, D. Koss, *Metall. Trans. A* 16A (1985) 675–681.
 - [90] M. Grange, J. Besson, E. Andrieu, *Int. J. Fract.* 105 (2000) 273–293.
 - [91] P. Bouffieux, N. Rupa, in: G.P. Sabol, G.D. Moan (Eds.), *Zirconium in the Nuclear Industry: Twelfth International Symposium*, ASTM STP 1354, American Society for Testing and Materials, 2000, pp. 399–422.
 - [92] N. Rupa, M. Clavel, P. Bouffieux, C. Domain, A. Legris, in: G.D. Moan, P. Rudling (Eds.), *Zirconium in the Nuclear Industry: Thirteenth International Symposium*, ASTM STP 1423, American Society for Testing and Materials, 2002, pp. 811–836.
 - [93] J.W. Demmel, *Applied Numerical Linear Algebra*, Society for Industrial and Applied Mathematics (SIAM), Philadelphia, 1997.
 - [94] J. Tien, A. Thompson, I. Bernstein, R. Richards, *Metall. Trans. A* 7A (1976) 821–829.
 - [95] D. Porter, K. Easterling, *Phase Transformations in Metals and Alloys*, Van Nostrand Reinhold, Wokingham, 1981.
 - [96] G. Sauthoff, *Z. Metal.* 67 (1976) 25–29.
 - [97] C.J.C. Carpenter, *J. Nucl. Mater.* 48 (1973) 264–266.
 - [98] W.J. Pardee, N.E. Paton, *Metall. Mater. Trans. A* 11A (1980) 1391–1400.
 - [99] G.T. Camacho, M. Ortiz, *Int. J. Solids Struct.* 33 (1996) 2899–2938.